Title: Comprehensive analysis of A-type lamin tail region for repairing the nuclear lamina

Yohei Kono [1, 2, 3], Chan-Gi Pack [4, 5], Takehiko Ichikawa [2], Arata Komatsubara [6], Stephen A. Adam [7], Loïc Rolas [8], Sussan Nourshargh [8], Ohad Medalia [9], Robert D. Goldman [7], Takeshi Fukuma [2], Hiroshi Kimura [1, 6], Takeshi Shimi [1, 2*]

Running Head: Lamin A tail region controls the localization to the rupture sites

Author Affiliation:

[1] Cell Biology Center, Institute of Innovative Research, Tokyo Institute of Technology, Yokohama, Japan.

[2] Nano Life Science Institute (WPI-NanoLSI), Kanazawa University, Kanazawa, Japan.

[3] Faculty of Frontier Engineering, Institute of Science and Engineering, Kanazawa University, Kanazawa, Japan.

[4] Convergence Medicine Research Center, Asan Institute for Life Science, Asan Medical Center, Seoul, Korea.

[5] Department of Biomedical Engineering, University of Ulsan College of Medicine, Seoul, Korea.

[6] School of Life Science and Technology, Tokyo Institute of Technology, Yokohama, Japan.

[7] Department of Cell and Developmental Biology, Feinberg School of Medicine, Northwestern University, Chicago, IL.

[8] Centre for Microvascular Research, William Harvey Research Institute, Faculty of Medicine and Dentistry, Queen Mary University of London, London, UK.

[9] Department of Biochemistry, University of Zurich, Zurich, Switzerland.

The corresponding author:

Takeshi Shimi, Ph.D., Nano Life Science Institute (WPI-NanoLSI), Kanazawa University, Kakuma-machi, Kanazawa, 920-1192, Japan.

Phone: +81-76-234-4540; E-mail: t-shimi@staff.kanazawa-u.ac.jp

Abstract

The nuclear lamina (NL) lines the inner nuclear membrane (INM) of the nuclear envelope (NE) to maintain nuclear structure in metazoan cells. The major NL components, the nuclear lamins contribute to the protection against NE rupture induced by mechanical stress. Lamin C (LC) but not lamin A (LA) is rapidly diffused from the nucleoplasm to sites of NE rupture induced by laser microirradiation in immortalized mouse embryonic fibroblasts (MEFs). However, the molecular mechanism for differentiating LA from LC with respect to the localization/accumulation at the rupture sites still remains unknown. In this study, we reveal by immunofluorescence, live-cell imaging and fluorescence correlation spectroscopy (FCS) that the CaaX motif, the second cleavage site and the LA-characteristic segment (LACS) regulate the localization of LA to the rupture sites. Our data suggest that Hutchinson–Gilford Progeria syndrome (HGPS) might exhibit the delay in localizing LA to the rupture sites through this mechanism.

Introduction

In eukaryotic cell nuclei, the nuclear envelope (NE) spatially separates the nuclear genome from the cytoplasm. The barrier function of the NE is due to two phospholipid bilayers of the inner and outer nuclear membranes (INM, ONM). The INM is in contact with chromatin at the nuclear side via INM proteins (Zullo *et al.*, 2012), whereas the ONM is connected with the cytoskeletal system through the linker of nucleoskeleton and cytoskeleton (LINC) complex (Crisp *et al.*, 2006), and is continuous with membranous organelles including the endoplasmic reticulum (ER) (Voeltz *et al.*, 2002). The nuclear lamina (NL) is closely apposed to the INM and associates with heterochromatin to support nuclear structure. Nuclear pore complexes (NPCs) fill holes formed by the INM-ONM fusion for nucleo-cytoplasmic transport and interact with euchromatin (Paine *et al.*, 1975).

The NL structure consists of the nuclear lamins and associated proteins (Foisner and Gerace, 1993). The lamins are type V intermediate filament proteins, which are subdivided into A-type lamins (lamins A [LA] and C [LC]) and B-type lamins (lamins B1 [LB1] and B2 [LB2]) (Gerace *et al.*, 1978; Gerace and Blobel, 1980). LA and LC are derived from the single gene *LMNA* by alternative splicing (Lin and Worman, 1993), whereas LB1 and LB2 are encoded by separate genes *LMNB1* and *LMNB2*, respectively (Höger *et al.*, 1990; Biamonti *et al.*, 1992; Lin and Worman, 1995; Maeno *et al.*, 1995). Lamin molecules assemble into a filament with a diameter of ~3.5 nm and these filaments appear to non-randomly lay on top of each other to form meshworks of the NL with a thickness of ~13.5 nm in immortalized mouse embryonic fibroblasts (MEFs) (Shimi *et al.*, 2015; Turgay *et al.*, 2017). LA/C and LB1 filaments associate with the outer ring structure of the NPC and are involved in regulating the distribution of the meshworks and NPCs (Shimi *et al.*, 2008; Shimi *et al.*, 2015; Turgay *et al.*, 2017; Kittisopikul *et al.*, 2021).

68 The −CaaX box at the C terminus of LA, LB1 and LB2 is post-translationally
69 processed in steps, including the attachment of farnesyl group to the cysteine residue of
70 the −CaaX box by a farnesyltransferase (Lutz *et al.*, 1992; Sinensky *et al.*, 1994),
71 proteolytic cleavage of three residues (−aaX) by an aaX endopeptidase (Boyartchuk *et al.*,
72 1997) and carboxyl methylation of the terminal carboxylic acid group (−COOH) of the
73 C-terminal cysteine residue by a carboxyl methyltransferase (Winter-Vann and Casey,
74 2005). The maturation of LB1 and LB2 is completed by these steps. In case of the
75 farnesylated and carboxymethylated pre-LA, an additional 15 C-terminal residues
76 including the farnesylated and carboxymethylated cysteine, are cleaved off by
77 ZmpSte24/FACE1 to produce mature LA (Leung *et al.*, 2001; Corrigan *et al.*, 2005).
78 The NE is locally ruptured during physiological and pathological circumstances.
79 Immediately after NE rupture, NE components are recruited to the rupture sites with the
80 endosomal sorting complex required for transport-III (ESCRT-III) complex and Barrier-
81 to-autointegration factor (BAF) (Denais *et al.*, 2016; Raab *et al.*, 2016; Halfmann *et al.*,
82 2019). Nuclear DNA adjacent to the rupture sites is recognized by the DNA sensors cyclic
83 GMP-AMP synthase (cGAS) and its downstream signaling effector STING (Denais *et al.*,
84 2016; Raab *et al.*, 2016; Halfmann *et al.*, 2019). The frequency of spontaneous and forced
85 NE rupture is significantly increased by the depletion of lamins (Vargas *et al.*, 2012;
86 Robijns *et al.*, 2016; Chen *et al.*, 2018; Chen *et al.*, 2019). Numerous mutations have been
87 found throughout the *LMNA* gene that cause a spectrum of human genetic disorders,
88 collectively called laminopathies. Laminopathies associated with dilated cardiomyopathy
89 (DCM), muscular dystrophy (MD), familial partial lipodystrophy (FPLD) and
90 Hutchinson–Gilford Progeria syndrome (HGPS) are frequently accompanied by
91 spontaneous NE rupture (De Vos *et al.*, 2011; Earle *et al.*, 2020; Kim *et al.*, 2021). In

92 HGPS, the heterozygous transversion of a nucleotide substitution at position 1824 T>C
93 (G608G) leads to abnormal splicing of the last 150 nucleotides of exon 11, resulting in
94 the expression of progerin (PG) which lacks 50 amino acids (residues 607–656) from the
95 C terminus of pre-LA (Fig. 1 A). Because these residues contain the second proteolytic
96 cleavage site involved in pre-LA processing, PG remains farnesylated and
97 carboxymethylated, leading to its permanent association with the INM (De Sandre-
98 Giovannoli *et al.*, 2003; Eriksson *et al.*, 2003).

99 Recently, we found that LC but not LA was rapidly recruited from the
100 nucleoplasm to sites of NE rupture induced by laser microirradiation along with BAF in
101 immortalized MEFs (Kono *et al.*, 2022). However, the molecular mechanism by which
102 LA and LC differ in localization/accumulation kinetics at the rupture sites still remains to
103 be elucidated. Here, we investigate the involvement of LA processing in regulating lamin
104 localization within a relatively long-time window by immunofluorescence using MEFs
105 with wild type (WT) and HGPS backgrounds. Our previous study by live-cell imaging
106 demonstrated that the rapid accumulation of mEmerald-fused LA was observed only
107 when it was overexpressed at a high level (Kono *et al.*, 2022), and the accumulation
108 kinetics appeared to be artifactual because it was not confirmed by immunofluorescence
109 (Kono *et al.*, 2022). Therefore, we established the ectopic expression system for live-cell
110 imaging and fluorescence correlation spectroscopy (FCS) in which mEmerald-LA,
111 alternate forms of LA, and mEmerald-LC are maintained at a low level by expression
112 from the endogenous promotor in WT, HGPS and LA/C-knockout (KO) MEFs. Our data
113 reveal the significance of the CaaX motif, the second proteolytic cleavage site and the
114 LA-characteristic sequence (LACS) in the C-terminal tail region for regulating the
115 localization of LA at the rupture sites. We provide further insights into the molecular

116 mechanism that differentiate LA from LC for lamin localization/accumulation kinetics at

117 the rupture sites.

118 ## Results

119 **Localization of PG and LA to the rupture sites is delayed by PG expression**

120 To investigate the significance of the CaaX motif and the second cleavage site of pre-LA
121 for regulating the localization kinetics at the rupture sites, we used immortalized WT
122 MEFs and heterozygous knock-in MEFs with PG expression from a mutant allele of the
123 *Lmna* gene carrying the c.1827C>T; p.Gly609Gly mutation (*Lmna*$^{G609G/+}$, G609G/+).
124 This mutation is equivalent to the HGPS mutation in the human *LMNA* gene (Lopez-
125 Mejia *et al.*, 2011; Osorio *et al.*, 2011). These cells stably expressed super-folder Cherry
126 harboring two NLSs derived from SV40 large T antigen and c-Myc (NLS-sfCherry) as a
127 NE rupture marker (Kono *et al.*, 2022). Because spontaneous NE rupture is frequently
128 observed in skin fibroblasts derived from a HGPS patient (De Vos *et al.*, 2011), we first
129 examined if G609G/+ MEFs also exhibit misshapen nuclei, the leakage of NLS-sfCherry
130 to the cytoplasm, mislocalization of LB1 and cGAS accumulation, which are indicative
131 of spontaneous NE rupture. WT and G609G/+ cells were stained with Hoechst 33342 for
132 DNA and specific antibodies directed against LB1 and cGAS (Fig. S1 A). Unlike the
133 HGPS patient cells, G609G/+ cells did not show these phenotypes compared to WT cells
134 (Table S1), indicating that the HGPS mutation is not accompanied by spontaneous NE
135 rupture in these MEFs. Next, to examine the effect of this mutation on recovery from
136 forced NE rupture, single-cell compression by AFM indentation was applied to these cells,
137 and the nuclear reentry of NLS-sfCherry was observed by time-lapse imaging before and
138 after the induction of the rupture (Fig. 1 B) (Ivanovska *et al.*, 2023). Interestingly,
139 G609G/+ cells showed a significantly slow reentry compared to the WT cells which had
140 a ~50% recovery from the original fluorescence intensity ~4 min after the rupture (Fig. 1
141 C and D), indicating that PG expression slows the recovery from forced NE rupture.

142 To determine the localization kinetics of LA and PG at the rupture sites in WT
143 and G609G/+ nuclei, these cells were fixed at 30, 60 and 120 min after the induction of
144 NE rupture by 405-nm laser microirradiation (Fig. 1 E) (Kono *et al.*, 2022), and then
145 stained with Hoechst 33342 for DNA and specific antibodies directed against LA and PG,
146 which do not cross-react to each other (Fig. 1 A). LA was detected at the rupture sites in
147 ~54.5%, ~76.7% and ~85.7% of WT nuclei, and in ~28.6%, ~61.3% and ~67.6% of
148 G609G/+ nuclei within 30-40, 60-70 and 120-130 min after laser microirradiation,
149 respectively (Fig. 1 F and G, Fig. S1 B), strongly suggesting that PG expression slows
150 the localization kinetics of LA. Similarly, PG localization to the rupture sites was
151 determined in G609G/+ cells by immunofluorescence. PG was present at the rupture sites
152 in ~7.1%, ~32.3% and ~50.0% of G609G/+ nuclei (Fig. 1 G), indicating that the PG is
153 significantly slower in localizing to the rupture sites than LA in WT and G609G/+ cells.
154

155 **LC accumulation to the rupture sites is delayed by PG expression**

156 The slow localization of LA and PG to the rupture sites is unlikely to be directly linked
157 to the delay in retrieving NLS-sfCherry from the cytoplasm immediately after the
158 induction of NE rupture (Fig. 1 C, D, F and G). Because LC rapidly accumulates at the
159 rupture sites and the depletion slows the nuclear reentry of NLS-sfCherry at the early time
160 points (within 10 min) (Kono *et al.*, 2022), PG expression could slow LC accumulation.
161 To test this idea, endogenous LA, LC and PG were directly labeled with a LA/C-specific
162 genetically encoded probe, designed ankyrin repeat protein (DARPin)-LaA_6 (Zwerger
163 *et al.*, 2015), fused with super-folder GFP (sfGFP), sfGFP-DARPin-LA6 in WT and
164 G609G/+ MEFs expressing NLS-sfCherry (Kono *et al.*, 2022) (Fig. 2 A). Because
165 endogenous LA and PG did not localize to the rupture sites within 180 s after the induction

166 of NE rupture (Kono *et al.*, 2022) (Fig. 1 B and C, Fig. S1 B), sfGFP-DARPin-LA6
167 accumulating at the rupture sites only represented endogenous LC within the short-time
168 window. After laser microirradiation, the accumulation of sfGFP-DARPin-LA6 at the
169 rupture sites was significantly slower in G609G/+ cells compared to WT cells (Fig. 2 B
170 and C), indicating that PG expression reduced LC accumulation.

171 Because nucleoplasmic LC diffuses to the rupture sites (Kono *et al.*, 2022), the
172 diffusion fraction could be decreased in G609G/+ cells compared to WT cells. To test this
173 idea, the diffusion fraction and time of mEmerald-LC were quantitatively measured by
174 fluorescence correlation spectroscopy (FCS) (Fig. 2 D) (Shimi *et al.*, 2008; Kochin *et al.*,
175 2014; Shimi *et al.*, 2016). Because the low expression level of mEmerald-LC was
176 required for FCS measurement, it was stably expressed from a single allele of the *Rosa26*
177 locus with endogenous *Lmna* promotor in WT and G609G/+ MEFs (Fig. S2 A and B).
178 The auto-correlation curve obtained by the signal detection was fitted with fast and slow
179 components (Shimi *et al.*, 2008; Kochin *et al.*, 2014; Shimi *et al.*, 2016). Interestingly,
180 the diffusion coefficient of the fast component, at 37.8% in WT cells was significantly
181 larger than that at 45.0% in G609G/+ cells (Fig. 2 E): ~20.1 ± 1.0 $\mu m^2/s$ and ~12.1 ± 0.8
182 $\mu m^2/s$ in WT and G609G/+ nuclei, respectively, indicating that PG expression reduced
183 the diffusion speed of mEmerald-LC. These results from FCS measurement could explain
184 in part the slow accumulation of sfGFP-DARPin-LA6 at the rupture sites in G609G/+
185 cells.

186

187 **Inhibition of CaaX motif farnesylation increases the localization of LA and PG to**
188 **the rupture sites**

189 Because the CaaX motifs of pre-LA and PG are farnesylated (Holtz *et al.*, 1989; Sinensky
190 *et al.*, 1994), they are retained at the NE through the hydrophobic interaction with the
191 lipid bilayer of the INM (Holtz *et al.*, 1989; Gelb *et al.*, 2006). Therefore, the localization
192 of farnesylated pre-LA and PG to the rupture sites could be significantly decreased
193 compared to the non-farnesylated forms. To check this possibility, WT and G609G/+
194 MEFs were treated with DMSO or farnesyltransferase inhibitor (FTI), 3.2 μM lonafarnib
195 for 48 h, and farnesylation levels of pre-LA and PG were determined by immunoblotting
196 and immunofluorescence using specific antibodies directed against pre-LA, mature-LA
197 and PG, which do not cross-react to each other (Fig. S3 A). According to previous studies,
198 the pre-LA antibody appears to have preference for recognizing non-farnesylated pre-LA
199 compared to farnesylated pre-LA by western blotting but not immunofluorescence (Lee
200 *et al.*, 2010; Chang *et al.*, 2012; Yao *et al.*, 2020; Chen *et al.*, 2021). The pre- and mature-
201 LA expression levels were significantly increased and decreased in FTI-treated cells
202 compared to DMSO-treated cells, respectively (Fig. 3 A and S3 B). FTI-treated WT and
203 G609G/+ cells had a higher abundance of LA and PG in the average fluorescence intensity
204 of the nucleoplasmic pool relative to that of the NL (NP/NL ratio) than those treated with
205 DMSO (Fig. 3 B and S3 B). The NP/NL ratio of pre-LA was even higher than that of LA
206 in these FTI-treated cells (Fig. 3 B). These results indicate that LA and PG are increased
207 in the nucleoplasmic pool and/or decreased at the NL by FTI treatment (Fig. 3 B).
208 These cells were fixed 60 min after laser microirradiation and the localization of
209 LA and PG to the rupture sites was detected by immunofluorescence. LA was localized
210 to the rupture sites in ~59.5%, ~91.4%, ~42.1% and ~73.5% of DMSO-and FTI-treated
211 WT and G609G/+ nuclei, respectively, and pre-LA in ~94.3% and ~76.5% of FTI-treated
212 WT and G609G/+ nuclei (Fig. 3 C). PG was localized to the rupture sites in ~17.6% and

213 ~81.3% of DMSO-and FTI-treated G609G/+ nuclei (Fig. 3 C), as observed in non-treated
214 cells, respectively (Fig. 1 C and D). These results indicate that FTI treatment significantly
215 increases the localization of LA and PG at the rupture sites.

216 The increase in localization of LA and PG to the rupture sites by FTI treatment
217 was accompanied by an increase in NP/NL ratios (Fig. 3 B and C). Therefore, FTI
218 treatment could also increase the diffusion fraction and time of LA and PG in WT and
219 G609G/+ MEFs. To test this idea, the diffusion fraction and time of mEmerald-LA and
220 PG were measured by FCS. For FCS measurements, mEmerald-LA or PG was stably
221 expressed at a low level from a single allele of the *Rosa26* locus with endogenous *Lmna*
222 promotor in WT and G609G/+ MEFs, followed by the treatment with DMSO or FTI (Fig.
223 S2 A, B and S3 C). As expected, the diffusion coefficient of the fast component in
224 G609G/+ cells was significantly smaller than that in WT cells: ~19.7 ± 1.0 $\mu m^2/s$, ~17.3
225 ± 0.7 $\mu m^2/s$, ~16.0 ± 0.8 $\mu m^2/s$ and ~17.4 ± 0.7 $\mu m^2/s$ in DMSO- and FTI-treated WT and
226 G609G/+ nuclei, respectively (Fig. 3 E). These results show that PG expression reduced
227 the diffusion speed of mEmerald-LA. The diffusion signals of mEmerald-PG were barely
228 detectable in the nucleoplasm of WT and G609G/+ nuclei treated with DMSO. Instead,
229 the decay signals, which appeared to originate from the NL were detected during FCS
230 measurement because is the lamins are immobile in the NL (Dahl *et al.*, 2006). When WT
231 and G609G/+ cells were treated with the FTI, the diffusion signals were detected by FCS:
232 ~38.3% and ~42.2% of the fast component and ~61.7% and ~57.8% of the slow
233 component in FTI-treated WT and G609G/+ nuclei, respectively (Fig. 3 F). These results
234 indicate that PG becomes diffusible in the nucleoplasm by FTI treatment, and is the likely
235 source of PG localized to the rupture sites.
236

237 **The second proteolytic cleavage is required for the localization of LA to the rupture**
238 **sites**

239 Because the localization of PG to the rupture sites was significantly decreased compared
240 to LA (Fig. 1 C and D), the second cleavage site missing from PG could be also involved
241 in increasing pre-LA accumulation. Zmpste24 is involved in endoproteolytic processing
242 of the both the CaaX motif and second cleavage site (Quigley *et al.*, 2013). To test this
243 idea, we employed Zmpste24 knockdown (KD) in WT MEFs by lentivirus-mediated
244 expression of short hairpin RNAs (shRNAs). The expression levels of Zmpste24 and pre-
245 LA were determined in cells expressing shRNAs for the control (Scramble) or Zmpste24
246 KD (shZmpste24) by immunoblotting and immunofluorescence. The additional 15 C-
247 terminal residues including the CaaX motif remained partially uncleaved by Zmpste24
248 KD, resulting in the significant increase and decrease in expression level of and pre-LA
249 and mature-LA, as shown as the upper and lower band, respectively (Fig. 4 A). These
250 results are consistent with the previous findings to indicate that Zmpste24 KD inhibits the
251 second proteolytic cleavage (Yu *et al.*, 2013). LA and pre-LA were predominantly
252 localized to the NL, and the NP/NL ratios remained unchanged in Zmpste24-KD cells
253 compared to the control cells (Fig. 4 B and C). This value is similar to that of pre-LA in
254 Zmpste24-KD cells (Fig. 4 C).

255 These cells were fixed within 60 min after laser microirradiation, and then the
256 localization of LA and pre-LA to the rupture sites were determined by
257 immunofluorescence. LA was localized at the rupture sites in ~75% of the control cells
258 whereas LA and pre-LA were completely absent from the rupture sites in Zmpste24-KD
259 cells (Fig. 4 D and E), indicating that the second cleavage is required for increasing the
260 localization of LA.

261

262 **Inhibition of farnesylation at the CaaX motif is sufficient for the localization of LA**
263 **to the rupture sites without the second proteolytic cleavage**

264 Zmpste24 depletion significantly increased pre-LA expression (Fong *et al.*, 2004) (Fig.
265 5A and B), which is accompanied by farnesylation at the CaaX motif (Lee *et al.*, 2010).
266 Therefore, the inhibition of the farnesylation with FTI could release the pre-LA from the
267 NL, resulting in increasing the localization at the rupture sites. To test this idea, the control
268 and Zmpste24-KD cells were treated with DMSO or FTI as before, and the expression
269 levels and localization of pre-LA and mature-LA were determined by immunoblotting
270 and immunofluorescence (Fig. 5 A and B). As expected, the pre- and mature-LA
271 expression levels were significantly increased and decreased in the control and Zmpste24-
272 KD cells by FTI treatment, respectively (Fig. 5 A and B). Zmpste24 KD also induced the
273 same effect as the FTI treatment, and both of them together had most significant effect
274 among all the combinations (Fig. 5 A and B). The difference in sensitivity between
275 immunoblotting and indirect immunofluorescence of anti-pre-LA antibody (7G11) may
276 be due to specific physical constraints caused by the close proximity of the 7G11 epitope
277 to the farnesylation site rather than the presence of farnesylation (Chang *et al.*, 2012;
278 Casasola *et al.*, 2016; Yao *et al.*, 2020). The combination of pre- and mature-LA was
279 predominantly localized to the NL in these cells (Fig. 5 B). Among them, Zmpste24-KD
280 cells had the lowest NP/NL ratio of pre-LA with DMSO treatment and the highest of
281 mature-LA with FTI treatment (Fig. 5 C and D).

282 The localization of pre- and mature-LA to the rupture sites was determined by
283 immunofluorescence. Pre-LA was localized to the rupture sites in ~96.9%, ~11.8% and
284 ~77.1% of FTI-treated control nuclei and Zmpste24-KD nuclei with DMSO or FTI

285 treatment, respectively (Fig. 5 E). Mature-LA was almost undetectable in laser-
286 microirradiated Zmpste24-KD nuclei, and localized to the rupture site in ~56.7% and
287 ~40.6% of DMSO- or FTI-treated control nuclei, respectively (Fig. 5 E). These results
288 indicate that FTI treatment significantly increased the localization of pre-LA but not
289 mature-LA. Therefore, the inhibition of farnesylation at the CaaX motif increases the
290 localization of LA to the rupture sites without the second proteolytic cleavage.
291
292 **BAF is required for recruiting LA to the rupture sites**
293 BAF binds to the immunoglobulin (Ig)-like fold (Ig-fold) domain in the C-terminal tail
294 region of LA/C (Samson *et al.*, 2018). However, LC but not LA is rapidly recruited to the
295 rupture sites with BAF because LC is more abundant in the nucleoplasm than LA (Kono
296 *et al.*, 2022). It is possible that the slow localization of LA to the rupture sites could be
297 also dependent on BAF within a relatively long-time window. To test this possibility, BAF
298 KD was carried out with two shRNAs (shBAF #1 and #2) (Kono *et al.*, 2022), and the
299 efficiencies of BAF KD were confirmed by immunoblotting and immunofluorescence
300 using WT MEFs expressing shRNA for the control (Scramble) or shBAF #1 and #2 (Fig.
301 6 A and B). The NP/NL ratio of LA remained unchanged by BAF-KD cells compared to
302 the control cells (Fig. 6 B and C).
303 These cells were fixed within 60 min after laser microirradiation, and then LA
304 localization was determined by immunofluorescence. As expected, LA was localized to
305 the rupture sites in ~60.6%, 10.0% and ~15.6% of the control and BAF-KD#1 and #2
306 nuclei, respectively (Fig. 6 D and E), indicating that BAF is required for recruiting LA to
307 the rupture sites.
308

309 **LA differs from LC in localization to the rupture sites through two specific**
310 **sequences in the tail region**

311 LA and LC are identical until residue 566 or 568 in human or mouse, respectively (Fig.
312 S4 A). After these residue, LC harbors a unique six amino acid residue whereas LA has
313 98 or 97 amino acid residues in human or mouse, respectively. Since the LC-specific six
314 amino acid sequence does not contribute to the rapid accumulation of LC at the rupture
315 site (Kono *et al.*, 2022), it is possible that there is the LA-characteristic segment (LACS)
316 that inhibit the rapid accumulation of LA to the rupture sites. To test this idea, LA/C-KO
317 MEFs were transfected with C-terminus truncated mEmerald-LAs, then live-cell imaged
318 after the induction of NE rupture by 405-nm laser microirradiation (Fig. 7 A). mEmerald-
319 LA-S575X had a significant increase in NP/NL ratio compared to mEmerald-LA-FL (Fig.
320 7 B and C). mEmerald-LA-S575X but not mEmerald-LA-A601X rapidly accumulated
321 within 180 s, indicating that the 26 amino acid sequence of residues 575-600 (LAΔ26)
322 between them is critical for delaying the accumulation (Fig. 7 D and S4 B). Next, because
323 the deletion mutant of the 26 amino acids identified above (mEmerald-LAΔ26) did not
324 accumulate to the rupture site within 180 s, further truncation was performed at the C-
325 terminal side of mEmerald-LAΔ26 (Fig.7 A). The NP/NL ratio of mEmerald-LAΔ26
326 remained unchanged until the C-terminal truncation at residue 627 (mEmerald-LAΔ26-
327 F627X) compared to the mEmerald-LA-FL (Fig. S4 C-E and S4 E), indicating that
328 residues 627-643 are critical for inhibiting the accumulation. We therefore designated
329 LAΔ26 as LA-characteristic sequence-1 (LACS1) and the 17 amino acid sequence
330 identified later (627-643) as LACS2.

331 **Discussion**

332 A-type lamins are recruited to sites of NE rupture to repair the NL (Denais *et al.*, 2016;
333 Raab *et al.*, 2016; Kono *et al.*, 2022). We previously showed that the recruitment of LC
334 was significantly earlier than that of LA and was not attributable to the unique six amino
335 acid segment at the C-terminus following the amino acid sequence shared between them
336 (Kono *et al.*, 2022). In this study, we analyze the pre-LA tail region extended from the
337 unique segment, and Fig. 8 summarizes our current findings following our previous study.
338 The CaaX motif, the second proteolytic cleavage site and two LACSs of the LA tail region
339 determine the abundance of the nucleoplasmic pool. Because of the recruitment from the
340 nucleoplasm to the rupture sites, the processing and binding of these regulatory segments
341 are likely to be rate-limiting steps for the localization kinetics at the rupture sites.

342 We use immortalized G609G/+ MEFs to analyze the CaaX motif and the second
343 cleavage site of pre-LA with respect to the localization at the rupture sites. Unlike HGPS
344 patient cells, G609G/+ cells do not exhibit spontaneous NE rupture, which could be due
345 to the immortalization process with SV40 large T antigen. In oncogene-induced
346 senescence, DNA protrusion from the nucleus and the leakage of nuclear contents are
347 coupled to the loss of LB1 (Shimi *et al.*, 2011; Ivanov *et al.*, 2013; Dou *et al.*, 2015). LB1
348 expression could also decrease when HGPS patient cells become prematurely senescent
349 (Scaffidi and Misteli, 2005). Therefore, spontaneous NE rupture might be induced by the
350 HGPS mutation because of premature senescence. Instead of spontaneous NE rupture,
351 we find that after forced NE rupture induced by AFM indentation, the nuclear reentry of
352 NLS-sfCherry is significantly slow in G609G/+ cells compared to WT cells. Our
353 comparison between WT and G609G/+ cells shows that PG is not only slower in
354 localizing to the rupture sites than LA but also delays LA localization and LC

355 accumulation probably because PG stably interacts with LA and LC to form a regularly
356 aligned filaments in the NL (Dahl *et al.*, 2006). These results suggest that the HGPS
357 mutation would impair the repair of NE rupture rather than the structural integrity of the
358 NE.

359 When farnesylation at the CaaX motif of LA and PG is inhibited by FTI
360 treatment, pre-LA and pre-PG are increased in the nucleoplasm and localized to the
361 rupture sites, indicating that the farnesylation process limits the localization to the rupture
362 sites regardless of the second proteolytic cleavage of LA. Furthermore, Zmpste24 KD
363 blocks the second cleavage, leading to the complete inhibition of pre-LA localization to
364 the rupture sites, and the effect of Zmpste24 KD on the localization is rescued by FTI
365 treatment. These results strongly suggest that the majority of pre-LA molecules are
366 farnesylated by Zmpste24 KD and that the farnesylated form cannot localize to the rupture
367 sites.

368 Our previous and current studies indicate that LA and LC are recruited to the
369 rupture sites with BAF (Kono *et al.*, 2022). Despite this common mechanism for the
370 recruitment between them, the recruitment of LA is significantly slower that of LC
371 because LC is more abundant in the nucleoplasm than LA (Kono *et al.*, 2022). This
372 sequential order is positively correlated with the molecular exchange rates in the NL
373 (Broers *et al.*, 1999; Dahl *et al.*, 2006), suggesting that BAF facilitates the assembly of
374 LA and LC into the NL to maintain nuclear structure during interphase. To support this
375 idea, our and other's results indicate that BAF KD reduces LA in the NL (Haraguchi *et*
376 *al.*, 2007; Haraguchi *et al.*, 2008).

377 Apart from the farnesylation at the CaaX motif and the inhibition of the second
378 proteolytic cleavage of pre-LA, we find that LACS1 and LACS2 in the tail region delay

379 the localization at the rupture sites. Because the truncation of LACS1 significantly
380 increases the nucleoplasmic pool, LA appears to be retained at the NL longer than LC
381 through LACS1. It is possible that LACS1 is involved in the retention by the formation
382 of LA filament (e.g. polymerization) in the NL or the interaction with NE components
383 including INM proteins and SUN1/2. On the other hand, LACS2 could independently
384 inhibit LA localization to the rupture sites and/or assist LACS1 function for the retention.
385 In addition to the chromatin-binding domain (CBD) of LA/C, residues 396-430,which
386 was determined using the LC tail region (Taniura *et al.*, 1995), these LACSs might bind
387 to histones as LA-specific CBDs (Schibler *et al.*, 2023).

388 In the context of HGPS, the farnesylation at the CaaX motif and lack of the
389 second proteolytic cleavage site significantly reduce the nucleoplasmic pol of PG, leading
390 to the slow localization of PG to the rupture sites compared to LA. This molecular
391 mechanism could be also critical for their access to active enhancers in the nuclear interior
392 (Ikegami *et al.*, 2020). The presence of PG can lead to increased NE instability but we do
393 not observe spontaneous NE rupture in G609G/+ cells. Nevertheless, our findings
394 implicate pathological significance of the defective repair of the NL as indicated by the
395 slow localization kinetics of PG at the rupture sites. The therapeutic effect of FTI
396 treatment appears to rescue from the repair defect by targeting the farnesylation at the
397 CaaX motif of PG. Therefore, the induction of spontaneous NE rupture and the rescuing
398 with FTI treatment need validating using the mouse model of HGPS in future studies.

399 ## Materials and methods

400 **Plasmid construction**

401 Two different NLSs derived from SV40 large T antigen (NLS^{SV40}; PKKKRKV) and c-
402 Myc (NLS^{Myc}; PAAKRVKLD) from pCDH-NLS^{SV40}-sfCherry-NLS^{Myc}-Blast (Kono *et*
403 *al.*, 2022) were ligated to pCDH-CMV-MCS-EF1-Hygro (plasmid #CD515B-1, System
404 Biosciences) using the Ligation-Convenience Kit (Nippon Gene) and designated as
405 pCDH-NLS^{SV40}-sfCherry-NLS^{Myc}-Hygro. The annealed oligonucleotides to express
406 shRNAs (ZmpSte24, TRCN0000366641; BAF#1, TRCN0000124958; BAF#2,
407 TRCN0000124955; Table S2, Broad Institute) was ligated into pLKO.3-blast (Kono *et*
408 *al.*, 2022) using the Ligation-Convenience Kit. The pX459-sfCherry CRISPR-Cas9
409 vector were generated from pSpCas9(BB)-2A-Puro (pX459) V2.0 (Addgene plasmid #
410 62988 ; http://n2t.net/addgene:62988 ; RRID:Addgene_62988; a gift from Feng Zhang).
411 The annealed oligonucleotides to express single-guide RNA (sgRNA) against the *Rosa26*
412 target sequence (Chu *et al.*, 2015) was ligated into pX459-sfCherry using the Ligation-
413 Convenience Kit and designated as pX459-sfCherry-sgRosa26-1.

414 We cloned a 1.6 kb genomic region upstream from start codon of mouse *Lmna*
415 as the endogenous promoter (-1407 to +249 bp from transcription start site) using
416 PrimeSTAR HS DNA Polymerase (Takara). Primers used in this study are listed in Table
417 S2. Mouse genomic DNA was extracted from cells by Proteinase K (Fungal; Invitrogen)
418 digestion according to the standard protocol and used for a PCR template. The CMV
419 promoter of mEmerald-C1 (Addgene plasmid # 53975 ; http://n2t.net/addgene:53975 ;
420 RRID:Addgene_53975; a gift from Michael Davidson) was replaced by a *Lmna* promoter
421 using the In-Fusion HD Cloning Kit (Clontech) and designated as pLmna-mEmerald-C1.
422 The mouse pre-LA cDNA was amplified from pPyCAG-LA-IP (Guo *et al.*, 2014) using
423 the KOD One PCR Master Mix -Blue- (Toyobo), cloned into pLmna-mEmerald-C1 using
424 the In-Fusion, and designated as pLmna-Em-LA. The mouse PG cDNA was generated by
425 PrimeSTAR Max DNA Polymerase (Takara) to skip 150 bp, closed by In-Fusion HD, and
426 designated as pLmna-Em-PG. The amino acid truncation mutants were generated by PCR
427 mutagenesis using PrimeSTAR Max or PrimeSTAR HS DNA Polymerase. The LACS1
428 deletion mutant (Δ26) was generated using PrimeSTAR Max to skip 78 bp, and closed by
429 In-Fusion HD. The pLmna-Em-LA and pLmna-Em-PG expression cassettes were
430 amplified by the KOD One, fused with bGHpA amplified from LSL-Cas9-Rosa26TV

431 (Addgene plasmid # 61408 ; http://n2t.net/addgene:61408 ; RRID:Addgene_61408; a gift
432 from Feng Zhang) and *Pac* I/*Sma* I digested LSL-Cas9-Rosa26TV by In-Fusion HD, and
433 designated as pLmna-Em-LA-R26Neo and pLmna-Em-PG-R26Neo, respectively. The
434 mouse LC cDNA was also generated by KOD One PCR and In-Fusion HD and designated
435 as pLmna-Em-LC-R26Neo.
436
437 **Cell culture**
438 MEFs isolated from WT and heterozygous c.1827C>T mutant (*Lmna*$^{G609G/+}$, G609G/+)
439 embryos at embryonic day 13.5 were generous gifts from Carlos López-Otín, Universidad
440 de Oviedo (Lopez-Mejia *et al.*, 2011; Osorio *et al.*, 2011). Primary MEFs were cultured
441 in modified DMEM (high glucose; Nacalai Tesque) containing 10% FBS (qualified;
442 Thermo Fisher), 4 mM L-glutamine, 100U/mL penicillin and 100 μg/mL streptomycin
443 (Sigma-Aldrich), and 20 mM 2-[4-(2-Hydroxyethyl)-1-piperazinyl] ethanesulfonic acid
444 (HEPES; Nacalai Tesque) at 37°C in a humidified multi-gas incubator with 3% O_2/5%
445 CO_2 (MCO-5M, Sanyo/Panasonic Healthcare). Cells were immortalized by transduction
446 with a retrovirus expressing SV40 large T antigen from pBABE-puro largeTcDNA
447 (Addgene plasmid # 14088 ; http://n2t.net/addgene:14088 ; RRID:Addgene_14088; a gift
448 from William Hahn) as previously described (Shimi *et al.*, 2015). After selection with 2
449 μg/ml puromycin (InvivoGen) for 4 d, immortalized WT and G609G/+ cells were
450 cultured in growth medium without HEPES at 37°C in a humidified chamber with 5%
451 CO_2.
452
453 **Lentiviral transduction**
454 For lentivirus-mediated stable introduction of NLS^{SV40}-sfCherry-NLS^{Myc}, we followed
455 the methods described previously (Kono *et al.*, 2022). Briefly, pVSV-G (PT3343-5,
456 Clontech) and psPAX2 (Addgene plasmid #12260; http://n2t.net/addgene:12260;
457 RRID:Addgene_12260; a gift from Didier Trono), together with a pCDH vector (pCDH-
458 NLS^{SV40}-sfCherry-NLS^{Myc}-Blast, pCDH-NLS^{SV40}-sfCherry-NLS^{Myc}-Hygro or pCDH-
459 sfGFP-DARPin-LA6-Hygro) in a 1:3:4 weight ratio of each plasmid was transfected into
460 ~80% confluent 293T cells (CRL-3216, ATCC) using Lipofectamine 3000 following the
461 manufacturer's instructions for lentivirus production. One day after the transfection, the
462 medium was replaced with fresh medium, which was harvested at 48 h after transfection.

463 For virus infection, MEFs were incubated with the virus-containing culture supernatants
464 with 4 μg/mL polybrene (Nacalai Tesque) for 24 h. Infected cells were selected by
465 incubation in medium containing 3 μg/mL blasticidin S or 200 μg/mL hygromycin B Gold
466 (InvivoGen) for 4 d.
467
468 **Live-cell imaging and NE rupture induction by laser microirradiation**
469 Culture medium was replaced with FluoroBrite (Thermo Fisher) containing 10% FBS, 4
470 mM L-glutamine, 100U/mL penicillin and 100 μg/mL streptomycin. For laser-
471 microirradiation and image collection, cells were set onto a heated stage (37°C; Tokai
472 Hit) with a CO_2-control system (Tokken) on a confocal microscope (FV1000, Olympus)
473 with a 60× PlanApo N (NA 1.4) oil lens operated by built-in software FLUOVIEW ver.
474 4.2 (Olympus). All live-cell images were collected using a main scanner (4% 488-nm
475 laser transmission; 30% 543-nm laser transmission; 2 μs/pixel; 512×512 pixels; pinhole
476 100 μm; 6× zoom; ~10 s/frame). After the first image was acquired, a 2 μm diameter spot
477 was laser-microirradiated using a second scanner at 100% power of 405-nm laser
478 transmission (40 μs/pixel; approximately 780 μW) for 10 s while the images were
479 collected with another scanner.
480 Fiji software (ImageJ) ver. 1.53v (National Institute of Health) was used for
481 measuring max intensity in the region of interest after Gaussian filtering with $\sigma = 2.0$ over
482 time. Fluorescence intensity was normalized by each of the initial intensity in the laser-
483 microirradiated region. CellProfiler ver. 3.1.9 (Broad Institute) with the
484 NP_NL_intensity_live pipeline (uploaded on GitHub; http://github.com/Kimura-
485 Lab/Kono-et-al.-2023) (Kono *et al.*, 2022) were used for measuring mean intensity of
486 mEmerald-LA mutants and mEmerald-LC in the NP and the NL. Briefly, after the nuclear
487 region was recognized by the nuclear localization of NLS-sfCherry, 3 pixels (207 nm)
488 and more than 10 pixels (690 nm) inside from the rim of nuclear region were regarded as
489 the NL and the NP, respectively, and then the mean intensity of each section was measured.
490 All images were processed in Photoshop ver. 24 (Adobe) for cropping and
491 brightness/contrast adjustment when applicable.
492
493 **Indirect immunofluorescence and microscopy**

494 Primary antibodies used for indirect immunofluorescence were mouse monoclonal anti-
495 LA (1:250; 4A58, sc-71481, Santa Cruz), rat monoclonal anti-pre-LA (1:1,000; 7G11;
496 MABT345, EMD Millipore; (Lee *et al.*, 2010)), mouse monoclonal anti-mature-LA
497 (1:8,000; 4A4-A4, 14-9848-82, Invitrogen; (Roblek *et al.*, 2010)), rabbit polyclonal anti-
498 progerin (1:1000; generated by the Nourshargh laboratory using a peptide immunogen of
499 murine progerin and standard immunization procedures; (Santiago-Fernández *et al.*,
500 2019; Marcos-Ramiro *et al.*, 2021; Sánchez-López *et al.*, 2021)) and rabbit monoclonal
501 anti-BANF1/BAF (1:200; EPR7668; ab129184, Abcam). The secondary antibodies used
502 were Alexa Fluor 488-donkey anti-mouse immunoglobulin G (IgG), Alexa Fluor 488-
503 donkey anti-rabbit IgG (1:2,000; A21202 and 1:2,000; A21206, respectively, Thermo
504 Fisher), Cy5-donkey anti-mouse IgG and Cy5-goat anti-rat IgG (1:2,000; 715-175-151
505 and 1:2,000; 712-175-153, respectively, Jackson ImmunoResearch).

506 Cells were grown on 35 mm Glass Based Dishes which have a cover glass with
507 a grid pattern (IWAKI) and fixed after laser-microirradiation with 4% PFA (Electron
508 Microscopy Sciences) containing 0.1% Triton X-100 (Nacalai Tesque) for 15 min,
509 followed by permeabilization using 0.1% Triton X-100 in PBS for 10 min and then
510 blocking with Blocking One-P (Nacalai Tesque) for 30 min. Cells were incubated with
511 primary antibodies overnight at 4°C, washed with 10% Blocking One-P in PBS, and
512 incubated with secondary antibodies for 1 h at RT. DNA was stained with Hoechst 33342
513 (0.5 μg/mL; Thermo Fisher). For Fig. S1 A, cells were fixed with 4% PFA for 15 min,
514 followed by permeabilization using 0.1% Triton X-100 in PBS for 10 min and then
515 blocking with Blocking One-P for 30 min. The RFP-Booster Alexa Fluor 568 (alpaca
516 monoclonal anti-RFP Nanobody; 1:1000; rb2AF568, ChromoTek) was used to amplify
517 the signal of NLS-sfCherry.

518 Confocal fluorescence images were obtained using a confocal microscope
519 FV1000 with a 60× PlanApo N (NA 1.4) oil lens (3.0% 405-nm laser transmission; 3.1-
520 11.1% 488-nm laser transmission; 5.0% 543-nm laser transmission; 1.0-4.0% 633-nm
521 laser transmission; 2 μs/pixel; 512×512 pixels; pinhole 100 μm). CellProfiler with the
522 NP_NL_intensity_fixed pipeline (uploaded on GitHub; http://github.com/Kimura-
523 Lab/Kono-et-al.-2023) were used for measuring mean intensity of lamins in the NP and
524 the NL. Briefly, after the nuclear region was recognized by the DNA, 3 pixels (207 nm)
525 and more than 10 pixels (690 nm) inside from the rim of nuclear region were regarded as

526 the NL and the NP, respectively, and then the mean intensity of each section was measured.
527 All images were processed in Photoshop ver. 24 for cropping and brightness/contrast
528 adjustment when applicable.
529
530 **Induction of mechanical NE rupture by atomic force microscopy (AFM)**
531 Culture medium was replaced with Leibovitz's L-15 medium (no phenol red; Thermo
532 Fisher) containing 10% FBS, 2 mM L-glutamine, 100U/mL penicillin and 100 μg/mL
533 streptomycin. JPK NanoWizard 4 BioAFM (Bruker) incorporated into an inverted
534 fluorescence microscope (Eclipse Ti2, Nikon) with EM-CCD camera (iXon Ultra 888,
535 Andor) and light source (X-Cite XYLIS, Excelitas) was used for single-cell compression.
536 Cantilever (TL-CONT, Nanosensors; spring constant approximately 0.2 N/m) with a 100
537 μm glass bead (BZ-01, As-One) was used for NE rupture. Cells expressing NLS-sfCherry
538 were set onto a heated stage (37°C) and the first fluorescent image of NLS-sfCherry was
539 obtained before the rupture using a TRITC filter and NIS-Elements BR (Nikon). Next,
540 the bead was approached on the top of the cell surface with 2 nN setpoint and then forced
541 down for 5 μm. After waiting for 10 s, the cantilever was retracted. Within 10 s after the
542 retraction, time-lapse imaging was started with 30 s exposure time every 30 s for 5 min.
543
544 **Chemicals**
545 As a selective farnesyltransferase inhibitor (FTI), lonafarnib (SCH66336; Merck) was
546 dissolved in dimethylsulfoxide (DMSO; Nacalai Tesque) and added to the cells with one
547 daily dose of 3.2 μM for 2 days. For controls in all experiments, an equal volume of
548 vehicle (0.1% DMSO) was added.
549
550 **Immunoblotting**
551 For immunoblotting, we followed the methods described previously (Kono et al., 2022).
552 Briefly, primary antibodies used for immunoblotting were mouse monoclonal anti-LA/C
553 (1:5,000-20,000; 3A6-4C11, 14-9847-82, eBioscience), rat monoclonal anti-pre-LA
554 (1:1,000; 7G11), mouse monoclonal anti-mature-LA (1:2,500; 4A4-A4), rabbit
555 polyclonal anti-progerin (1:1,000; Nourshargh lab), rabbit monoclonal anti-
556 BANF1/BAF (1:500; EPR7668, Abcam), anti-β-Actin (1:2,000; AC-15, sc-69879, Santa

557 Cruz) and anti-GAPDH (1:5,000; 6C5, sc-32233, Santa Cruz). The secondary antibodies
558 used were anti-mouse IgG HRP-linked whole Ab sheep (1:10,000; NA931, Amersham),
559 anti-rabbit IgG HRP-linked $F(ab')_2$ fragment donkey (1:10,000; NA9340, Amersham)
560 and HRP-donkey anti-rat IgG (H+L) (1:10,000; 712-035-150, Jackson ImmunoResearch).
561

562 **Rosa26-targeted gene knock-in**

563 The pLmna-Em-preLA-R26Neo, pLmna-Em-PG-R26Neo and pLmna-Em-LC-R26Neo
564 were linearized by the *Kpn* I (Takara) and purified by phenol/chloroform extraction and
565 ethanol precipitation. Cells were transfected with appropriate plasmids using
566 Lipofectamine 3000 (Thermo Fisher) by reverse transfection as previously described
567 (Kono *et al.*, 2022). Briefly, the DNA-lipid complex (3 μg linearized *Rosa26* targeting
568 vectors : 2 μg pX459-sfCherry-sgRosa26-1 : 7.5 μL Lipofectamine 3000 in 250 μL Opti-
569 MEM; Thermo Fisher) was added to 1.62×10^5 cells as they were seeding onto a 35 mm
570 dish with 2 mL of growth medium. One day after the transfection, the medium was
571 replaced with fresh medium. Two days after the transfection, cells were selected by
572 incubation in medium containing 400 μg/mL G-418 disulfate aqueous solution (Nacalai
573 Tesque) for 7 d.
574

575 **Fluorescence Correlation Spectroscopy (FCS)**

576 FCS measurements were all performed at 25°C with an LSM780 confocal microscope
577 (Carl Zeiss) as described previously (Shimi *et al.*, 2008; Park *et al.*, 2015; Shimi *et al.*,
578 2016). FCS setups using the LSM780 microscope consisted of a continuous-wave Ar^+
579 laser (25 mW), a water-immersion objective (C-Apochromat, ×40/1.2 NA; Carl Zeiss),
580 and a GaAsP multichannel spectral detector (Quasar; Carl Zeiss). Fluorescent protein of
581 mEmerald was excited with the 488-nm laser line with a minimal laser power (0.5%) to
582 allow an optimal signal-to-noise ratio. Diameter of pinhole was adjusted to 34 μm (1 Airy
583 unit) for the 488-nm laser. Emission fluorescence was detected at 500–550 nm in the
584 green channel. The structure parameter and detection volume were calibrated using
585 Rhodamine-6G (Sigma-Aldrich) solution with diffusion coefficient (280 $\mu m^2/s$; 25°C in
586 water) before cell experiment. For live cell analysis, three positions of FCS measurement
587 were selected in the nuclei of cells excluding the nucleoli. For FCS measurements,
588 measuring time and repetition were set to 10 s and 5 times, respectively. The first of five

589 repetitions were considered prebleach, and then four repetitions were used for further
590 analysis. FCS data were analyzed with analytical software installed in the ZEN 2012 SP5
591 FP1 (black) acquisition software (Carl Zeiss) (Park *et al.*, 2015; Shimi *et al.*, 2016).
592 Briefly, all measured fluorescence auto-correlation functions (FAFs) from live cells were
593 globally fitted by the ConfoCor3 software installed on LSM780 system using fitting
594 models considering three-dimensional free diffusion with a Gaussian laser profile,
595 including a triplet component to estimate the diffusion coefficient.
596
597 **Generation of the ZmpSte24- and BAF-KD MEFs**
598 MEFs expressing shRNAs of anti-ZmpSte24 and anti-BAF were generated through
599 lentiviral transduction. KD by shRNA expression was carried out by Lentivirus
600 transduction (see the section on Lentiviral transduction above) and 3 d selection with 3
601 μg/mL blasticidin S Gold for pLKO.3-blast.
602
603 **Statistical analyses**
604 Unless mentioned otherwise, all plots showed mean values ± SEM (error bars). Fisher's
605 exact test was performed to analyze the categorical data using EZR on R commander ver.
606 1.61 (programmed by Yoshinobu Kanda) (Kanda, 2013). The mixed effect model fit by
607 restricted maximum likelihood (REML) was performed to analyze the interaction
608 between group and time using the *lme4* (Bates *et al.*, 2015) and the *lmerTest* (Kuznetsova
609 *et al.*, 2017) packages in EZR, where cell's id was set as a random effect, while group and
610 time as fixed effects. The interaction between group and time (group × time) was also set
611 as a fixed effect. The Welch's t-test or the Welch's one-way ANOVA followed by the
612 Games–Howell post-hoc test was performed to single or multiple comparison,
613 respectively. Statistic codes for R ver. 4.2.2 and a modified R commander for EZR 1.61
614 are uploaded on GitHub (http://github.com/Kimura-Lab/Kono-et-al.-2023). Significance
615 was determined if $P < 0.05$.

616 **Supplemental material**

617 Table S1 shows the phenotype characterization in WT and G609G/+ MEFs by
618 immunofluorescence. Table S2 shows oligonucleotide sequences used in this study. Fig.
619 S1 shows the immunofluorescence of WT and G609G/+ MEFs for phenotype
620 characterization, and localization of LA and PG to NE rupture site at 30 and 120 min after
621 laser microirradiation. Fig. S2 shows the *Rosa26* knocked-in cells expressing A-type
622 lamins under Lmna promoter for FCS analysis. Fig. S3 shows the immunofluorescence,
623 immunoblotting and diffusion fraction in FTI-treated WT and G609G/+ MEFs. Fig. S4
624 shows the differences between LA and LC amino acid sequence, and dynamics of LA
625 mutants at the rupture sites, and the fluorescence intensities in the NP to the NL ratio of
626 mEmerald-LA mutants by live-cell imaging.

Acknowledgments

We would like to thank Prof. Carlos López-Otín (Universidad de Oviedo) for providing us with the primary MEFs isolated from WT and *Lmna* c.1827C>T mutant (*Lmna*$^{G609G/+}$ and *Lmna*$^{G609G/G609G}$) embryos. We thank Biomaterials Analysis Division, Open Facility Center (OFC) of Tokyo Institute of Technology for nucleotide sequencing and sharing research equipment, especially Carl Zeiss ElyraS1/Airyscan/LSM780 is shared in MEXT Project Grant Number JPMXS0440200021. We also thank the Cellular Imaging Core Facility at the ConveRgence mEDIcine research cenTer (CREDIT), Asan Medical Center for technical support. The generation and validation of the anti-murine progerin antibody was funded by the Wellcome Trust (098291/Z/12/Z to S. Nourshargh) and the British Heart Foundation (FS/IBSRF/22/25121 to L. Rolas). We also acknowledge the R statistic code generated by Shinsuke Hatano (Ryukoku University). We also thank all members of the Kimura lab at Tokyo Institute of Technology for advice and discussions. This work was supported by JSPS KAKENHI Grant Numbers JP20KK0158 (to T. Shimi, Y. Kono and H. Kimura), JP20K06617 (to T. Shimi), and JP18H05527 and JP21H04764 (to H. Kimura). This work was also supported by MEXT (World Premier International Research Center Initiative [WPI]). Y. Kono was an academy scholar at the Specialized Academy for Cell Science (Ohsumi-juku) of the Tokyo Tech Organization for Fundamental Research (OFR). The authors declare no competing financial interests.

Author contributions

T. Shimi conceived the project. Y. Kono designed, performed and interpreted experiments. C.G. Pack performed FCS experiments. T. Ichikawa performed AFM experiments. A. Komatsubara performed image analysis. L. Rolas and S. Nourshargh generated, characterized, and provided the anti-murine progerin antibody. S.A. Adam, O. Medalia and R.D. Goldman provided advice and scientific discussion. Y. Kono, C.G. Pack, T. Ichikawa and T. Shimi drafted the manuscript. S.A. Adam, R.D. Goldman, and H. Kimura edited the manuscript. T. Shimi, S.A. Adam, T. Fukuma, H. Kimura and R.D. Goldman supervised the experiments.

656 ## References

657 Bates, D., Mächler, M., Bolker, B.M., and Walker, S.C. (2015). Fitting Linear Mixed-Effects Models Using
658 lme4. Journal of Statistical Software *67*, 1-48.
659 Biamonti, G., Giacca, M., Perini, G., Contreas, G., Zentilin, L., Weighardt, F., Guerra, M., Della Valle, G.,
660 Saccone, S., Riva, S., and Falaschi, A. (1992). The gene for a novel human lamin maps at a highly
661 transcribed locus of chromosome 19 which replicates at the onset of S-phase. Mol Cell Biol *12*, 3499-3506.
662 Boyartchuk, V.L., Ashby, M.N., and Rine, J. (1997). Modulation of Ras and a-factor function by carboxyl-
663 terminal proteolysis. Science *275*, 1796-1800.
664 Broers, J.L.V., Machiels, B.M., van Eys, G.J.J.M., Kuijpers, H.J.H., Manders, E.M.M., van Driel, R., and
665 Ramaekers, F.C.S. (1999). Dynamics of the nuclear lamina as monitored by GFP-tagged A-type lamins. J
666 Cell Sci *112 (Pt 20)*, 3463-3475.
667 Casasola, A., Scalzo, D., Nandakumar, V., Halow, J., Recillas-Targa, F., Groudine, M., and Rincón-Arano,
668 H. (2016). Prelamin A processing, accumulation and distribution in normal cells and laminopathy disorders.
669 Nucleus *7*, 84-102.
670 Chang, S.Y., Hudon-Miller, S.E., Yang, S.H., Jung, H.J., Lee, J.M., Farber, E., Subramanian, T., Andres,
671 D.A., Spielmann, H.P., Hrycyna, C.A., Young, S.G., and Fong, L.G. (2012). Inhibitors of protein
672 geranylgeranyltransferase-I lead to prelamin A accumulation in cells by inhibiting ZMPSTE24. J Lipid Res
673 *53*, 1176-1182.
674 Chen, N.Y., Kim, P., Weston, T.A., Edillo, L., Tu, Y., Fong, L.G., and Young, S.G. (2018). Fibroblasts
675 lacking nuclear lamins do not have nuclear blebs or protrusions but nevertheless have frequent nuclear
676 membrane ruptures. Proc Natl Acad Sci U S A *115*, 10100-10105.
677 Chen, N.Y., Yang, Y., Weston, T.A., Belling, J.N., Heizer, P., Tu, Y., Kim, P., Edillo, L., Jonas, S.J., Weiss,
678 P.S., Fong, L.G., and Young, S.G. (2019). An absence of lamin B1 in migrating neurons causes nuclear
679 membrane ruptures and cell death. Proc Natl Acad Sci U S A *116*, 25870-25879.
680 Chen, X., Yao, H., Kashif, M., Revêchon, G., Eriksson, M., Hu, J., Wang, T., Liu, Y., Tüksammel, E.,
681 Strömblad, S., Ahearn, I.M., Philips, M.R., Wiel, C., Ibrahim, M.X., and Bergo, M.O. (2021). A small-
682 molecule ICMT inhibitor delays senescence of Hutchinson-Gilford progeria syndrome cells. Elife *10*.
683 Chu, V.T., Weber, T., Wefers, B., Wurst, W., Sander, S., Rajewsky, K., and Kühn, R. (2015). Increasing the
684 efficiency of homology-directed repair for CRISPR-Cas9-induced precise gene editing in mammalian cells.
685 Nat Biotechnol *33*, 543-548.
686 Corrigan, D.P., Kuszczak, D., Rusinol, A.E., Thewke, D.P., Hrycyna, C.A., Michaelis, S., and Sinensky,
687 M.S. (2005). Prelamin A endoproteolytic processing in vitro by recombinant Zmpste24. Biochem J *387*,
688 129-138.
689 Crisp, M., Liu, Q., Roux, K., Rattner, J.B., Shanahan, C., Burke, B., Stahl, P.D., and Hodzic, D. (2006).
690 Coupling of the nucleus and cytoplasm: role of the LINC complex. J Cell Biol *172*, 41-53.

691 Dahl, K.N., Scaffidi, P., Islam, M.F., Yodh, A.G., Wilson, K.L., and Misteli, T. (2006). Distinct structural
692 and mechanical properties of the nuclear lamina in Hutchinson-Gilford progeria syndrome. Proc Natl Acad
693 Sci U S A *103*, 10271-10276.
694 De Sandre-Giovannoli, A., Bernard, R., Cau, P., Navarro, C., Amiel, J., Boccaccio, I., Lyonnet, S., Stewart,
695 C.L., Munnich, A., Le Merrer, M., and Lévy, N. (2003). Lamin a truncation in Hutchinson-Gilford progeria.
696 Science *300*, 2055.
697 De Vos, W.H., Houben, F., Kamps, M., Malhas, A., Verheyen, F., Cox, J., Manders, E.M.M., Verstraeten,
698 V.L.R.M., van Steensel, M.A.M., Marcelis, C.L.M., van den Wijngaard, A., Vaux, D.J., Ramaekers, F.C.S.,
699 and Broers, J.L.V. (2011). Repetitive disruptions of the nuclear envelope invoke temporary loss of cellular
700 compartmentalization in laminopathies. Hum Mol Genet *20*, 4175-4186.
701 Denais, C.M., Gilbert, R.M., Isermann, P., McGregor, A.L., te Lindert, M., Weigelin, B., Davidson, P.M.,
702 Friedl, P., Wolf, K., and Lammerding, J. (2016). Nuclear envelope rupture and repair during cancer cell
703 migration. Science *352*, 353-358.
704 Dou, Z., Xu, C., Donahue, G., Shimi, T., Pan, J.A., Zhu, J., Ivanov, A., Capell, B.C., Drake, A.M., Shah,
705 P.P., Catanzaro, J.M., Ricketts, M.D., Lamark, T., Adam, S.A., Marmorstein, R., Zong, W.X., Johansen, T.,
706 Goldman, R.D., Adams, P.D., and Berger, S.L. (2015). Autophagy mediates degradation of nuclear lamina.
707 Nature *527*, 105-109.
708 Earle, A.J., Kirby, T.J., Fedorchak, G.R., Isermann, P., Patel, J., Iruvanti, S., Moore, S.A., Bonne, G.,
709 Wallrath, L.L., and Lammerding, J. (2020). Mutant lamins cause nuclear envelope rupture and DNA
710 damage in skeletal muscle cells. Nat Mater *19*, 464-473.
711 Eriksson, M., Brown, W.T., Gordon, L.B., Glynn, M.W., Singer, J., Scott, L., Erdos, M.R., Robbins, C.M.,
712 Moses, T.Y., Berglund, P., Dutra, A., Pak, E., Durkin, S., Csoka, A.B., Boehnke, M., Glover, T.W., and
713 Collins, F.S. (2003). Recurrent de novo point mutations in lamin A cause Hutchinson-Gilford progeria
714 syndrome. Nature *423*, 293-298.
715 Foisner, R., and Gerace, L. (1993). Integral Membrane-Proteins of the Nuclear-Envelope Interact with
716 Lamins and Chromosomes, and Binding Is Modulated by Mitotic Phosphorylation. Cell *73*, 1267-1279.
717 Fong, L.G., Ng, J.K., Meta, M., Coté, N., Yang, S.H., Stewart, C.L., Sullivan, T., Burghardt, A., Majumdar,
718 S., Reue, K., Bergo, M.O., and Young, S.G. (2004). Heterozygosity for Lmna deficiency eliminates the
719 progeria-like phenotypes in Zmpste24-deficient mice. Proc Natl Acad Sci U S A *101*, 18111-18116.
720 Gelb, M.H., Brunsveld, L., Hrycyna, C.A., Michaelis, S., Tamanoi, F., Van Voorhis, W.C., and Waldmann,
721 H. (2006). Therapeutic intervention based on protein prenylation and associated modifications. Nat Chem
722 Biol *2*, 518-528.
723 Gerace, L., and Blobel, G. (1980). The nuclear envelope lamina is reversibly depolymerized during mitosis.
724 Cell *19*, 277-287.
725 Gerace, L., Blum, A., and Blobel, G. (1978). Immunocytochemical localization of the major polypeptides
726 of the nuclear pore complex-lamina fraction. Interphase and mitotic distribution. J Cell Biol *79*, 546-566.

727 Guo, Y., Kim, Y., Shimi, T., Goldman, R.D., and Zheng, Y. (2014). Concentration-dependent lamin
728 assembly and its roles in the localization of other nuclear proteins. Mol Biol Cell *25*, 1287-1297.
729 Halfmann, C.T., Sears, R.M., Katiyar, A., Busselman, B.W., Aman, L.K., Zhang, Q., O'Bryan, C.S.,
730 Angelini, T.E., Lele, T.P., and Roux, K.J. (2019). Repair of nuclear ruptures requires barrier-to-
731 autointegration factor. J Cell Biol *218*, 2136-2149.
732 Haraguchi, T., Kojidani, T., Koujin, T., Shimi, T., Osakada, H., Mori, C., Yamamoto, A., and Hiraoka, Y.
733 (2008). Live cell imaging and electron microscopy reveal dynamic processes of BAF-directed nuclear
734 envelope assembly. J Cell Sci *121*, 2540-2554.
735 Haraguchi, T., Koujin, T., Osakada, H., Kojidani, T., Mori, C., Masuda, H., and Hiraoka, Y. (2007). Nuclear
736 localization of barrier-to-autointegration factor is correlated with progression of S phase in human cells. J
737 Cell Sci *120*, 1967-1977.
738 Höger, T.H., Zatloukal, K., Waizenegger, I., and Krohne, G. (1990). Characterization of a second highly
739 conserved B-type lamin present in cells previously thought to contain only a single B-type lamin.
740 Chromosoma *99*, 379-390.
741 Holtz, D., Tanaka, R.A., Hartwig, J., and McKeon, F. (1989). The CaaX motif of lamin A functions in
742 conjunction with the nuclear localization signal to target assembly to the nuclear envelope. Cell *59*, 969-
743 977.
744 Ikegami, K., Secchia, S., Almakki, O., Lieb, J.D., and Moskowitz, I.P. (2020). Phosphorylated Lamin A/C
745 in the Nuclear Interior Binds Active Enhancers Associated with Abnormal Transcription in Progeria. Dev
746 Cell *52*, 699-713 e611.
747 Ivanov, A., Pawlikowski, J., Manoharan, I., van Tuyn, J., Nelson, D.M., Rai, T.S., Shah, P.P., Hewitt, G.,
748 Korolchuk, V.I., Passos, J.F., Wu, H., Berger, S.L., and Adams, P.D. (2013). Lysosome-mediated processing
749 of chromatin in senescence. J Cell Biol *202*, 129-143.
750 Ivanovska, I.L., Tobin, M.P., Bai, T., Dooling, L.J., and Discher, D.E. (2023). Small lipid droplets are rigid
751 enough to indent a nucleus, dilute the lamina, and cause rupture. J Cell Biol *222*.
752 Kanda, Y. (2013). Investigation of the freely available easy-to-use software 'EZR' for medical statistics.
753 Bone Marrow Transplant *48*, 452-458.
754 Kim, P.H., Chen, N.Y., Heizer, P.J., Tu, Y., Weston, T.A., Fong, J.L.C., Gill, N.K., Rowat, A.C., Young, S.G.,
755 and Fong, L.G. (2021). Nuclear membrane ruptures underlie the vascular pathology in a mouse model of
756 Hutchinson-Gilford progeria syndrome. JCI Insight *6*.
757 Kittisopikul, M., Shimi, T., Tatli, M., Tran, J.R., Zheng, Y., Medalia, O., Jaqaman, K., Adam, S.A., and
758 Goldman, R.D. (2021). Computational analyses reveal spatial relationships between nuclear pore
759 complexes and specific lamins. J Cell Biol *220*.
760 Kochin, V., Shimi, T., Torvaldson, E., Adam, S.A., Goldman, A., Pack, C.G., Melo-Cardenas, J., Imanishi,
761 S.Y., Goldman, R.D., and Eriksson, J.E. (2014). Interphase phosphorylation of lamin A. J Cell Sci *127*,
762 2683-2696.

763 Kono, Y., Adam, S.A., Sato, Y., Reddy, K.L., Zheng, Y., Medalia, O., Goldman, R.D., Kimura, H., and
764 Shimi, T. (2022). Nucleoplasmic lamin C rapidly accumulates at sites of nuclear envelope rupture with
765 BAF and cGAS. J Cell Biol *221*.
766 Kuznetsova, A., Brockhoff, P.B., and Christensen, R.H.B. (2017). lmerTest Package: Tests in Linear Mixed
767 Effects Models. Journal of Statistical Software *82*, 1-26.
768 Lee, R., Chang, S.Y., Trinh, H., Tu, Y., White, A.C., Davies, B.S., Bergo, M.O., Fong, L.G., Lowry, W.E.,
769 and Young, S.G. (2010). Genetic studies on the functional relevance of the protein prenyltransferases in
770 skin keratinocytes. Hum Mol Genet *19*, 1603-1617.
771 Leung, G.K., Schmidt, W.K., Bergo, M.O., Gavino, B., Wong, D.H., Tam, A., Ashby, M.N., Michaelis, S.,
772 and Young, S.G. (2001). Biochemical studies of Zmpste24-deficient mice. J Biol Chem *276*, 29051-29058.
773 Lin, F., and Worman, H.J. (1993). Structural organization of the human gene encoding nuclear lamin A and
774 nuclear lamin C. J Biol Chem *268*, 16321-16326.
775 Lin, F., and Worman, H.J. (1995). Structural organization of the human gene (LMNB1) encoding nuclear
776 lamin B1. Genomics *27*, 230-236.
777 Lopez-Mejia, I.C., Vautrot, V., De Toledo, M., Behm-Ansmant, I., Bourgeois, C.F., Navarro, C.L., Osorio,
778 F.G., Freije, J.M., Stévenin, J., De Sandre-Giovannoli, A., Lopez-Otin, C., Lévy, N., Branlant, C., and Tazi,
779 J. (2011). A conserved splicing mechanism of the LMNA gene controls premature aging. Hum Mol Genet
780 *20*, 4540-4555.
781 Lutz, R.J., Trujillo, M.A., Denham, K.S., Wenger, L., and Sinensky, M. (1992). Nucleoplasmic localization
782 of prelamin A: implications for prenylation-dependent lamin A assembly into the nuclear lamina. Proc Natl
783 Acad Sci U S A *89*, 3000-3004.
784 Maeno, H., Sugimoto, K., and Nakajima, N. (1995). Genomic structure of the mouse gene (Lmnb1)
785 encoding nuclear lamin B1. Genomics *30*, 342-346.
786 Marcos-Ramiro, B., Gil-Ordóñez, A., Marín-Ramos, N.I., Ortega-Nogales, F.J., Balabasquer, M., Gonzalo,
787 P., Khiar-Fernández, N., Rolas, L., Barkaway, A., Nourshargh, S., Andrés, V., Martín-Fontecha, M., López-
788 Rodríguez, M.L., and Ortega-Gutiérrez, S. (2021). Isoprenylcysteine Carboxylmethyltransferase-Based
789 Therapy for Hutchinson-Gilford Progeria Syndrome. ACS Cent Sci *7*, 1300-1310.
790 Mirdita, M., Schütze, K., Moriwaki, Y., Heo, L., Ovchinnikov, S., and Steinegger, M. (2022). ColabFold:
791 making protein folding accessible to all. Nat Methods *19*, 679-682.
792 Osorio, F.G., Navarro, C.L., Cadiñanos, J., López-Mejía, I.C., Quirós, P.M., Bartoli, C., Rivera, J., Tazi, J.,
793 Guzmán, G., Varela, I., Depetris, D., de Carlos, F., Cobo, J., Andrés, V., De Sandre-Giovannoli, A., Freije,
794 J.M., Lévy, N., and López-Otín, C. (2011). Splicing-directed therapy in a new mouse model of human
795 accelerated aging. Sci Transl Med *3*, 106ra107.
796 Paine, P.L., Moore, L.C., and Horowitz, S.B. (1975). Nuclear envelope permeability. Nature *254*, 109-114.
797 Park, H., Han, S.S., Sako, Y., and Pack, C.G. (2015). Dynamic and unique nucleolar microenvironment
798 revealed by fluorescence correlation spectroscopy. FASEB J *29*, 837-848.

799 Quigley, A., Dong, Y.Y., Pike, A.C., Dong, L., Shrestha, L., Berridge, G., Stansfeld, P.J., Sansom, M.S.,
800 Edwards, A.M., Bountra, C., von Delft, F., Bullock, A.N., Burgess-Brown, N.A., and Carpenter, E.P. (2013).
801 The structural basis of ZMPSTE24-dependent laminopathies. Science *339*, 1604-1607.
802 Raab, M., Gentili, M., de Belly, H., Thiam, H.R., Vargas, P., Jimenez, A.J., Lautenschlaeger, F., Voituriez,
803 R., Lennon-Duménil, A.M., Manel, N., and Piel, M. (2016). ESCRT III repairs nuclear envelope ruptures
804 during cell migration to limit DNA damage and cell death. Science *352*, 359-362.
805 Robijns, J., Molenberghs, F., Sieprath, T., Corne, T.D.J., Verschuuren, M., and De Vos, W.H. (2016). In
806 silico synchronization reveals regulators of nuclear ruptures in lamin A/C deficient model cells. Sci Rep *6*,
807 30325.
808 Roblek, M., Schüchner, S., Huber, V., Ollram, K., Vlcek-Vesely, S., Foisner, R., Wehnert, M., and Ogris, E.
809 (2010). Monoclonal antibodies specific for disease-associated point-mutants: lamin A/C R453W and
810 R482W. PLoS One *5*, e10604.
811 Samson, C., Petitalot, A., Celli, F., Herrada, I., Ropars, V., Le Du, M.H., Nhiri, N., Jacquet, E., Arteni, A.A.,
812 Buendia, B., and Zinn-Justin, S. (2018). Structural analysis of the ternary complex between lamin A/C,
813 BAF and emerin identifies an interface disrupted in autosomal recessive progeroid diseases. Nucleic Acids
814 Res *46*, 10460-10473.
815 Sánchez-López, A., Espinós-Estévez, C., González-Gómez, C., Gonzalo, P., Andrés-Manzano, M.J., Fanjul,
816 V., Riquelme-Borja, R., Hamczyk, M.R., Macías, A., Del Campo, L., Camafeita, E., Vázquez, J., Barkaway,
817 A., Rolas, L., Nourshargh, S., Dorado, B., Benedicto, I., and Andrés, V. (2021). Cardiovascular Progerin
818 Suppression and Lamin A Restoration Rescue Hutchinson-Gilford Progeria Syndrome. Circulation *144*,
819 1777-1794.
820 Santiago-Fernández, O., Osorio, F.G., Quesada, V., Rodríguez, F., Basso, S., Maeso, D., Rolas, L.,
821 Barkaway, A., Nourshargh, S., Folgueras, A.R., Freije, J.M.P., and López-Otín, C. (2019). Development of
822 a CRISPR/Cas9-based therapy for Hutchinson-Gilford progeria syndrome. Nat Med *25*, 423-426.
823 Scaffidi, P., and Misteli, T. (2005). Reversal of the cellular phenotype in the premature aging disease
824 Hutchinson-Gilford progeria syndrome. Nat Med *11*, 440-445.
825 Schibler, A.C., Jevtic, P., Pegoraro, G., Levy, D.L., and Misteli, T. (2023). Identification of epigenetic
826 modulators as determinants of nuclear size and shape. Elife *12*, 10.1101/2022.1105.1128.493845.
827 Shimi, T., Butin-Israeli, V., Adam, S.A., Hamanaka, R.B., Goldman, A.E., Lucas, C.A., Shumaker, D.K.,
828 Kosak, S.T., Chandel, N.S., and Goldman, R.D. (2011). The role of nuclear lamin B1 in cell proliferation
829 and senescence. Genes Dev *25*, 2579-2593.
830 Shimi, T., Kittisopikul, M., Tran, J., Goldman, A.E., Adam, S.A., Zheng, Y., Jaqaman, K., and Goldman,
831 R.D. (2015). Structural organization of nuclear lamins A, C, B1, and B2 revealed by superresolution
832 microscopy. Mol Biol Cell *26*, 4075-4086.
833 Shimi, T., Pack, C.G., and Goldman, R.D. (2016). Analyses of the Dynamic Properties of Nuclear Lamins
834 by Fluorescence Recovery After Photobleaching (FRAP) and Fluorescence Correlation Spectroscopy

835 (FCS). Methods Mol Biol *1411*, 99-111.
836 Shimi, T., Pfleghaar, K., Kojima, S., Pack, C.G., Solovei, I., Goldman, A.E., Adam, S.A., Shumaker, D.K.,
837 Kinjo, M., Cremer, T., and Goldman, R.D. (2008). The A- and B-type nuclear lamin networks:
838 microdomains involved in chromatin organization and transcription. Genes Dev *22*, 3409-3421.
839 Sinensky, M., Fantle, K., Trujillo, M., McLain, T., Kupfer, A., and Dalton, M. (1994). The processing
840 pathway of prelamin A. J Cell Sci *107 (Pt 1)*, 61-67.
841 Taniura, H., Glass, C., and Gerace, L. (1995). A chromatin binding site in the tail domain of nuclear lamins
842 that interacts with core histones. J Cell Biol *131*, 33-44.
843 Turgay, Y., Eibauer, M., Goldman, A.E., Shimi, T., Khayat, M., Ben-Harush, K., Dubrovsky-Gaupp, A.,
844 Sapra, K.T., Goldman, R.D., and Medalia, O. (2017). The molecular architecture of lamins in somatic cells.
845 Nature *543*, 261-264.
846 Vargas, J.D., Hatch, E.M., Anderson, D.J., and Hetzer, M.W. (2012). Transient nuclear envelope rupturing
847 during interphase in human cancer cells. Nucleus *3*, 88-100.
848 Voeltz, G.K., Rolls, M.M., and Rapoport, T.A. (2002). Structural organization of the endoplasmic reticulum.
849 EMBO Rep *3*, 944-950.
850 Winter-Vann, A.M., and Casey, P.J. (2005). Post-prenylation-processing enzymes as new targets in
851 oncogenesis. Nat Rev Cancer *5*, 405-412.
852 Yao, H., Chen, X., Kashif, M., Wang, T., Ibrahim, M.X., Tüksammel, E., Revêchon, G., Eriksson, M., Wiel,
853 C., and Bergo, M.O. (2020). Targeting RAS-converting enzyme 1 overcomes senescence and improves
854 progeria-like phenotypes of ZMPSTE24 deficiency. Aging Cell *19*, e13200.
855 Yu, K.R., Lee, S., Jung, J.W., Hong, I.S., Kim, H.S., Seo, Y., Shin, T.H., and Kang, K.S. (2013). MicroRNA-
856 141-3p plays a role in human mesenchymal stem cell aging by directly targeting ZMPSTE24. J Cell Sci
857 *126*, 5422-5431.
858 Zullo, J.M., Demarco, I.A., Piqué-Regi, R., Gaffney, D.J., Epstein, C.B., Spooner, C.J., Luperchio, T.R.,
859 Bernstein, B.E., Pritchard, J.K., Reddy, K.L., and Singh, H. (2012). DNA sequence-dependent
860 compartmentalization and silencing of chromatin at the nuclear lamina. Cell *149*, 1474-1487.
861 Zwerger, M., Roschitzki-Voser, H., Zbinden, R., Denais, C., Herrmann, H., Lammerding, J., Grütter, M.G.,
862 and Medalia, O. (2015). Altering lamina assembly reveals lamina-dependent and -independent functions
863 for A-type lamins. J Cell Sci *128*, 3607-3620.
864

865 **Abbreviations**

866 BAF, barrier-to-autointegration factor; CBD, chromatin-binding domain; cGAS, cyclic
867 GMP-AMP synthase; DARPin, designed ankyrin repeat protein; DCM, dilated
868 cardiomyopathy; ESCRT-III, endosomal sorting complex required for transport-III; ER,
869 endoplasmic reticulum; FAF, fluorescence auto-correlation function; FCS, fluorescence
870 correlation spectroscopy; FTI, farnesyltransferase inhibitor; FPLD, familial partial
871 lipodystrophy; HGPS, Hutchinson-Gilford Progeria syndrome; Ig-fold, immunoglobulin-
872 like fold; INM, inner nuclear membrane; KD, knockdown; KO, knockout; LA, lamin A;
873 LACS, LA-characteristic segment; LB1, lamin B1; LB2, lamin B2; LC, lamin C; LINC,
874 linker of nucleoskeleton and cytoskeleton; MEF, mouse embryonic fibroblast; MD,
875 muscular dystrophy; NE, nuclear envelope; NL, nuclear lamina; non-p-BAF, non-
876 phosphorylated BAF; NP, nucleoplasmic pool; NPC, nuclear pore complex; ONM, outer
877 nuclear membrane; p-BAF, phosphorylated BAF; PG, progerin; REML, restricted
878 maximum likelihood; sfGFP, superfolder GFP; sfCherry, superfolder Cherry; shRNA,
879 short hairpin RNA; STING, stimulator of interferon genes; WT, wild type.

880 ## Figure legends

881 Figure 1. **The localization kinetics of LA and PG at sites of NE rupture induced by**
882 **laser microirradiation in WT and G609G/+ MEFs. (A)** Protein architecture of LA and
883 PG. The coiled-coil central rod domain (gray), the NLS (yellow), the β-strand comprising
884 the IG-fold (blue), and the CaaX motif box (orange) are shown. Anti-LA antibody (4A58)
885 and anti-PG antibody (RaPG) recognize LA- and PG-specific region, respectively, and
886 they do not cross-react with each other. Anti-pre-LA antibody (7G11) recognize the
887 adjacent site to the second proteolytic cleavage site, so do not cross-react with PG. **(B)**
888 AFM is used to induce forced NE rupture. **(C)** Time-lapse images of NLS-sfCherry
889 expressed in WT and G609G/+ MEFs before and after NE rupture induced by AFM
890 indentation. The fluorescence intensities are indicated with rainbow color. Bar: 10 μm.
891 **(D)** The nuclear-to-cytoplasmic intensity (N/C) ratio of NLS-sfCherry was measured and
892 normalized to the initial intensities, and plotted to monitor NE rupture (means ± SEM; n
893 = 20 cells from two independent experiments; ***, $P < 0.001$ from WT by a mixed effect
894 model). **(E)** A 405-nm laser is used to induce NE rupture at a precise location on the NL.
895 13 to 21 cells are irradiated within 10 min, then incubated for 30, 60 and 120 min followed
896 by fixation with 4% PFA/0.1% Triton-X 100. **(F** and **G)** A 2-μm diameter spot at the NE
897 in cells was lase microirradiated to induce NE rupture, fixed at 30-130 min after
898 incubation, and then stained with a combination of rabbit and mouse antibodies, followed
899 by Alexa Fluor 488-labeled anti-rabbit and Cy5-labeled anti-mouse IgG, and Hoechst
900 33342 for DNA. Two independent experiments were performed. **(F)** Representative
901 images of single confocal sections of WT and G609G/+ cells fixed within 60-70 min after
902 laser microirradiation. Magnified views of the indicated areas by orange boxes are shown
903 (bottom). The ruptured sites are indicated with yellow arrowheads (bottom). Bars: 5 μm
904 (top) and 2μm (bottom). **(G)** Ratios of cells with (blue) and without (gray) localization of
905 the indicated antibodies at NE rupture sites. The numbers of analyzed cells are indicated
906 in the bar charts.
907
908 Figure 2. Repair of NE rupture and **rapid accumulation of LC at the rupture sites in**
909 **WT and G609G/+ MEFs. (A)** Protein architecture of LA, LC and PG with sfGFP-
910 DARPin-LA6. The summary of their dynamics is indicated on the right (+, accumulated
911 at the rupture site; -, not accumulated). The structural image of sfGFP-DARPin-LA6 was
912 predicted by AlphaFold2 (Mirdita *et al.*, 2022) and edited by the PyMOL (Schrödinger).
913 **(B** and **C)** The sfGFP-DARPin-LA6 intensity at the rupture sites were measured with 10
914 s intervals, and the relative intensities are plotted (means ± SEM; n = 20 cells from two
915 independent experiments). **(B)** Dynamics of the sfGFP-DARPin-LA6 in response to NE
916 rupture in WT and G609G/+ cells. Magnified views of the indicated areas by orange
917 boxes are shown (the second to fifth columns). A 2-μm diameter spot was laser-

918 microirradiated to induce NE rupture (yellow arrowheads). Bars: 5 μm (the first column)
919 and 2 μm (the second to fifth columns). **(C)** Fluorescence intensities of sfGFP-DARPin-
920 LA6 at the rupture sites were measured and normalized to the initial intensities. ***, P <
921 0.001 from WT by a mixed effect model). **(D** and **E)** The diffusion fraction of mEmerald-
922 LC in WT and G609G/+ cells were measured by FCS. **(D)** A representative fluorescence
923 image of mEmerald-LC before FCS measurements (top). The yellow crosses indicate the
924 points measured by FCS. Bar, 10 μm. FCS measurements based on fluctuation analysis
925 of fluorescence intensity. mEmerald-LC (Em-LC) move in or out of the confocal volume
926 (white-out cylinder region in blue) at different speeds (bottom). **(E)** Diffusion coefficient
927 of fast (Component 1; plotted in black) and slow component (Component 2; plotted in
928 gray), mean ± SEM. Percentage of these components are indicated on the left to plots.
929 ***, P < 0.001 compared to WT of Component 1 by a Welch's t-test.
930
931 Figure 3. **The localization kinetics at the rupture sites in FTI-treated WT and**
932 **G609G/+ MEFs. (A)** Whole cell lysates from the indicated cells with 0.1% DMSO or
933 3.2 μM lonafarnib (FTI) were probed with anti-LA/C (3A6-4C11), anti-pre-LA (7G11),
934 anti-mature-LA (4A4-A4), anti-PG, and anti-GAPDH (as loading control). Positions of
935 the size standards are shown on the right. **(B)** Fluorescence intensities in the NP to the
936 NL ratio of the anti-LA (4A58), anti-pre-LA (7G11) and anti-PG was measured after
937 indirect immunofluorescence. ***, P < 0.001 compared to WT by a Welch's t-test. See
938 Fig. S3 B for microscopic image. **(C)** Ratios of cells with (blue) and without (gray)
939 localization of the indicated antibodies at NE rupture sites. The numbers of analyzed cells
940 are indicated in the bar charts. **(D-F)** The diffusion fraction of mEmerald-LA (Em-LA)
941 and mEmerald-PG (Em-PG) in WT and G609G/+ cells were measured by FCS. **(D)**
942 Representative fluorescence fluctuations of each mEmerald-tagged lamins in the
943 nucleoplasm plotted by count rate (green line for Em-LA and blue line for Em-PG) in WT
944 (top) and G609G/+ cells (bottom). **(E** and **F)** Diffusion coefficient of fast (Component 1;
945 plotted in black) and slow component (Component 2; plotted in gray) of Em-LA **(E)** and
946 Em-PG **(F)** in indicated cells. Percentage of these components are indicated on the left to
947 plots. N/A, not applicable because of pre-bleached. *, P < 0.05 from WT DMSO to
948 G609G/+ DMSO of Component 1 by a Games–Howell test.
949
950 Figure 4. **The localization kinetics at the rupture sites in ZmpSte24-KD WT MEFs.**
951 **(A)** Whole cell lysates from control (Scramble) and ZmpSte24-KD (shZmpste24) WT
952 cells were probed with anti-pre-LA (7G11), anti-LA/C (3A6-4C11) and anti-GAPDH (as
953 loading control). Positions of the size standards are shown on the right. **(B)** Scramble and
954 shZmpste24 WT cells were indirect immunofluorescent stained with anti-LA (4A58) and
955 anti-pre-LA (7G11). **(C)** Fluorescence intensities in the NP to the NL ratio of the anti-LA
956 (4A58) and anti-pre-LA (7G11) were measured. **(D)** Representative images of single

957 confocal sections of Scramble and shZmpste24 WT cells fixed within 60-70 min after
958 laser microirradiation. The ruptured sites with (blue arrowheads) or without (magenta
959 arrowheads) localization of antibodies are indicated. Bar: 40 μm. **(E)** Ratios of cells with
960 (blue) and without (gray) localization of the indicated antibodies at NE rupture sites. The
961 numbers of analyzed cells are indicated in the bar charts.
962
963 Figure 5. **The localization kinetics at the rupture sites in FTI-treated ZmpSte24-KD**
964 **WT MEFs. (A)** Whole cell lysates from the control (Scramble) and ZmpSte24-KD
965 (shZmpste24) cells with 0.1% DMSO or 3.2 μM lonafarnib (FTI) were probed with anti-
966 LA/C (3A6-4C11), anti-pre-LA (7G11), anti-mature-LA (4A4-A4), and anti-GAPDH (as
967 loading control). Positions of the size standards are shown on the right. **(B)** Representative
968 images of single confocal sections of Scramble and shZmpste24 WT cells with DMSO or
969 FTI. Bar: 5 μm. **(C** and **D)** Fluorescence intensities in the NP to the NL ratio of the anti-
970 pre-LA (7G11; **C**) and anti-mature-LA (4A4-A4; **D**) were measured. ***, $P < 0.001$ by a
971 Games–Howell test. **(E)** Ratios of cells with (blue) and without (gray) localization of the
972 indicated antibodies at NE rupture sites. The numbers of analyzed cells are indicated in
973 the bar charts.
974
975 Figure 6. **The localization kinetics at the rupture sites in BAF-KD WT MEFs. (A)**
976 Whole cell lysates from the control (Scramble) and BAF-KD (shBAF#1 and #2) cells
977 were probed with anti-BANF1/BAF (EPR7668) and anti-GAPDH (as loading control).
978 Positions of the size standards are shown on the right. **(B)** Representative images of single
979 confocal sections of Scramble, shBAF#1 and #2 WT cells. Bar: 5 μm. **(C)** Fluorescence
980 intensities in the NP to the NL ratio of the anti-LA (4A58) were measured. ***, $P < 0.001$
981 by a Games–Howell test. **(D)** Representative images of single confocal sections of
982 Scramble, shBAF#1 and #2 WT cells fixed within 60-70 min after laser microirradiation.
983 The ruptured sites with (blue arrowheads) or without (magenta arrowheads) localization
984 of anti-LA are indicated. Bar: 40 μm. **(E)** Ratios of cells with (blue) and without (gray)
985 localization of the indicated antibodies at NE rupture sites. The numbers of analyzed cells
986 are indicated in the bar charts.
987
988 Figure 7. **Rapid accumulation of LA with C-terminal and internal deletion mutants**
989 **at the rupture sites in LA/C-KO MEFs. (A)** Architecture of the deletion mutants of
990 mEmerald-LA expressed from *Lmna* promoter vector. Terminal amino acids are
991 numbered, and their accumulation dynamics is summarized on the right (+, accumulated
992 at the rupture site; -, not accumulated). **(B)** Representative images of single confocal
993 sections of mEmerald-LA-full-length (FL), L648X, T644X, F627X, S617X, A601X,
994 S575X, and mEmerald-LC in LA/C-KO MEFs transfected for 2 d. Bar: 5 μm. **(C)**
995 Fluorescence intensities in the NP to the NL ratio of mEmerald-LA mutants and

996 mEmerald-LC, as control, were measured. *, P < 0.05 and ‡, P<0.001 compared to all
997 others by a Games–Howell test. **(D)** Fluorescence intensities of mEmerald-LA with C-
998 terminal deletion mutants and mEmerald-LC, as control, at the rupture sites were
999 measured and normalized to the initial intensities. ***, P < 0.001 from LA-FL by a mixed
1000 effect model). **(E)** Fluorescence intensities of mEmerald-LA with internal and C-terminal
1001 deletion mutants at the rupture sites were measured and normalized to the initial
1002 intensities. ***, P < 0.001 from LA-FL by a mixed effect model). LA-FL and LC are
1003 reproduction of D.
1004
1005 Figure 8. **Schematic diagram of fast accumulation and slow localization of A-type**
1006 **lamins. (A)** NE rupture and the rapid accumulation of LC (green) and later localization
1007 of LA (magenta) and PG (yellow) are depicted. Phosphorylated BAF (p-BAF) forms
1008 complexes with LA, PG and LC, and rapidly accumulates at NE rupture site. LA is slower
1009 to accumulate than LC because it contains two LACS in the tail (top). PG is difficult to
1010 accumulate because it has a farnesylated C-terminus (top). When cells are treated with
1011 FTI, PG accumulates as well as LA because it has non-farnesylated C-terminus, but they
1012 still accumulate slower than LC because of LACS (bottom).

1013 Figure S1. **Phenotype characterization and the localization dynamics of LA and PG**
1014 **at the rupture sites in WT and G609G/+ MEFs. (A)** Phenotype characterization of WT
1015 and G609G/+ MEFs by immunofluorescence. Asterisk indicates cell with NE rupture due
1016 to the cell cycle and were excluded from the analysis. The misshapen, NE ruptured, mis-
1017 localized and cGAS accumulated nuclei are indicated with magenta arrowheads in DNA,
1018 NLS-sfCherry, anti-LB1 and anti-cGAS, respectively. **(B)** Representative images of
1019 single confocal sections of WT and G609G/+ cells fixed within 30-40 min (top) and 120-
1020 130 min (bottom) after laser microirradiation. Magnified views of the indicated areas by
1021 orange boxes are shown (bottom of each row). The ruptured sites are indicated with
1022 yellow arrowheads (bottom of each row). Bars: 5 μm (top of each row) and 2 μm (bottom
1023 of each row).
1024
1025 Figure S2. ***Rosa26*** **knock-in cells expressing A-type lamins under** ***Lmna*** **promoter for**
1026 **FCS analysis. (A)** The schematic diagram of linearized pLmna-Em-LA-R26Neo,
1027 pLmna-Em-PG-R26Neo and pLmna-Em-LC-R26Neo knock-in vectors. **(B)** Whole cell
1028 lysates from the indicated cells knocked-in with pLmna-Em-LA-R26Neo, pLmna-Em-
1029 PG-R26Neo and pLmna-Em-LC-R26Neo were probed with anti-LA/C (3A6-4C11) and
1030 anti-β-actin (as loading control). Positions of the size standards are shown on the right.
1031 **(C)** The diffusion fraction of Em-LC in WT and G609G/+ cells. ***, $P < 0.001$ from WT
1032 to G609G/+ by a Welch's t-test.
1033
1034 Figure S3. **The immunofluorescence, immunoblotting and diffusion fraction in FTI-**
1035 **treated WT and G609G/+ MEFs. (A)** Protein architecture of LA and PG with
1036 recognition regions of post-translational processing specific antibodies. Anti-mature-LA
1037 (4A4-A4) and anti-pre-LA (7G11) do not cross-react with each other and PG. **(B)** WT and
1038 G609G/+ MEFs treated with 0.1% DMSO (top) and 3.2 μM lonafarnib (FTI, bottom)
1039 were indirect immunofluorescent stained with anti-LA (4A58), anti-pre-LA (7G11) and
1040 anti-PG (RaPG). Bar: 5 μm. **(C)** Whole cell lysates from the indicated cells knocked-in
1041 with pLmna-Em-LA-R26Neo and pLmna-Em-PG-R26Neo treated with DMSO or FTI
1042 were probed with anti-LA/C (3A6-4C11) and anti-GAPDH (as loading control). Positions
1043 of the size standards are shown on the right. **(D)** The diffusion fraction of Em-LA and
1044 Em-PG in WT and G609G/+ cells. N/A, not applicable because of pre-bleached. **, $P <$
1045 0.01, ***, $P < 0.001$ by a Games–Howell test.
1046
1047 Figure S4. **Accumulation dynamics of LA with C-terminal and internal deletion**
1048 **mutants at the rupture sites in LA/C-KO MEFs. (A)** Amino acid sequences of LA-
1049 (blue) or LC-specific (red) regions from *Homo sapiens* and *Mus musculus*. The amino
1050 acid homology is indicated as bars and a gap introduced between residue A600 and A601
1051 to maximize homology. **(B)** Dynamics of the mEmerald-LA-S575X and A601X in

1052 response to NE rupture in LA/C-KO MEFs. **(C)** Representative images of single confocal
1053 sections of mEmerald-LA-full-length (FL), LA-FL without LACS1 (LAΔ26), LAΔ26-
1054 L648X, LAΔ26-T644X, LAΔ26-F627X, and mEmerald-LC in LA/C-KO cells
1055 transfected for 2 d. Bar: 5 μm. **(D)** Fluorescence intensities in the NP to the NL ratio of
1056 mEmerald-LA mutants and mEmerald-LC, as control, were measured. ***, $P < 0.001$ by
1057 a Steel–Dwass test. **(E)** Dynamics of the mEmerald-LAΔ26-T644X and LAΔ26-F627X
1058 in response to NE rupture in LA/C-KO cells. **(B** and **E)** Magnified views of the indicated
1059 areas by orange boxes are shown (the second to fifth columns). A 2-μm diameter spot
1060 was laser-microirradiated to induce NE rupture (yellow arrowheads). Bars: 5 μm (the first
1061 column) and 2 μm (the second to fifth columns).

Fig. 1

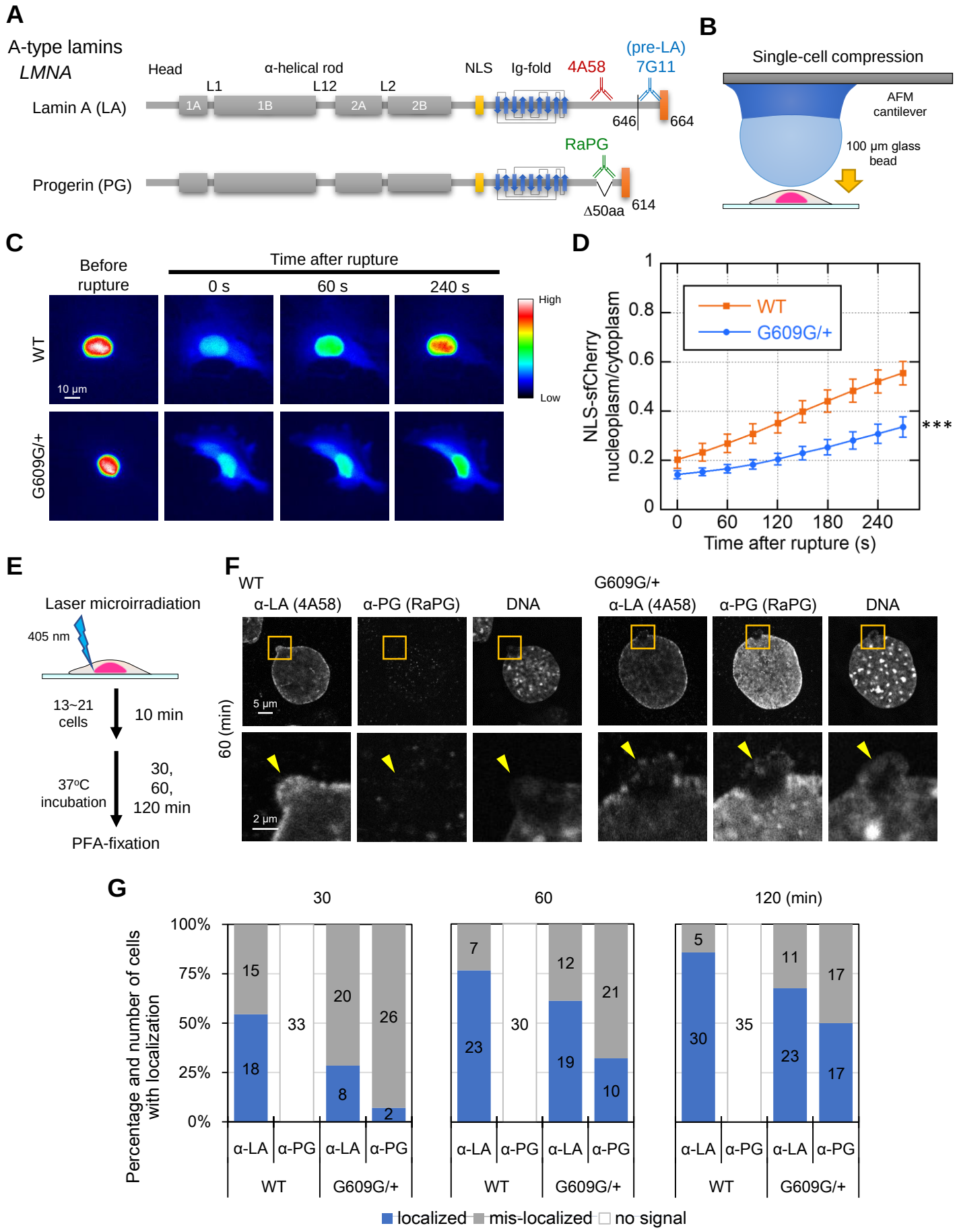
A
A-type lamins
LMNA
Head
α-helical rod
L1
L12
L2
NLS
Ig-fold
4A58
(pre-LA)
7G11
Lamin A (LA)
1A
1B
2A
2B
646
664
RaPG
Progerin (PG)
Δ50aa
614
B
Single-cell compression
AFM cantilever
100 μm glass bead
C
Before rupture
Time after rupture
0 s
60 s
240 s
WT
G609G/+
10 μm
High
Low
D
WT
G609G/+
NLS-sfCherry nucleoplasm/cytoplasm
Time after rupture (s)
***
E
Laser microirradiation
405 nm
13~21 cells
10 min
37°C incubation
30, 60, 120 min
PFA-fixation
F
WT
G609G/+
α-LA (4A58)
α-PG (RaPG)
DNA
60 (min)
5 μm
2 μm
G
30
60
120 (min)
Percentage and number of cells with localization
100%
75%
50%
25%
0%
α-LA
α-PG
WT
G609G/+
localized
mis-localized
no signal

Fig. 2

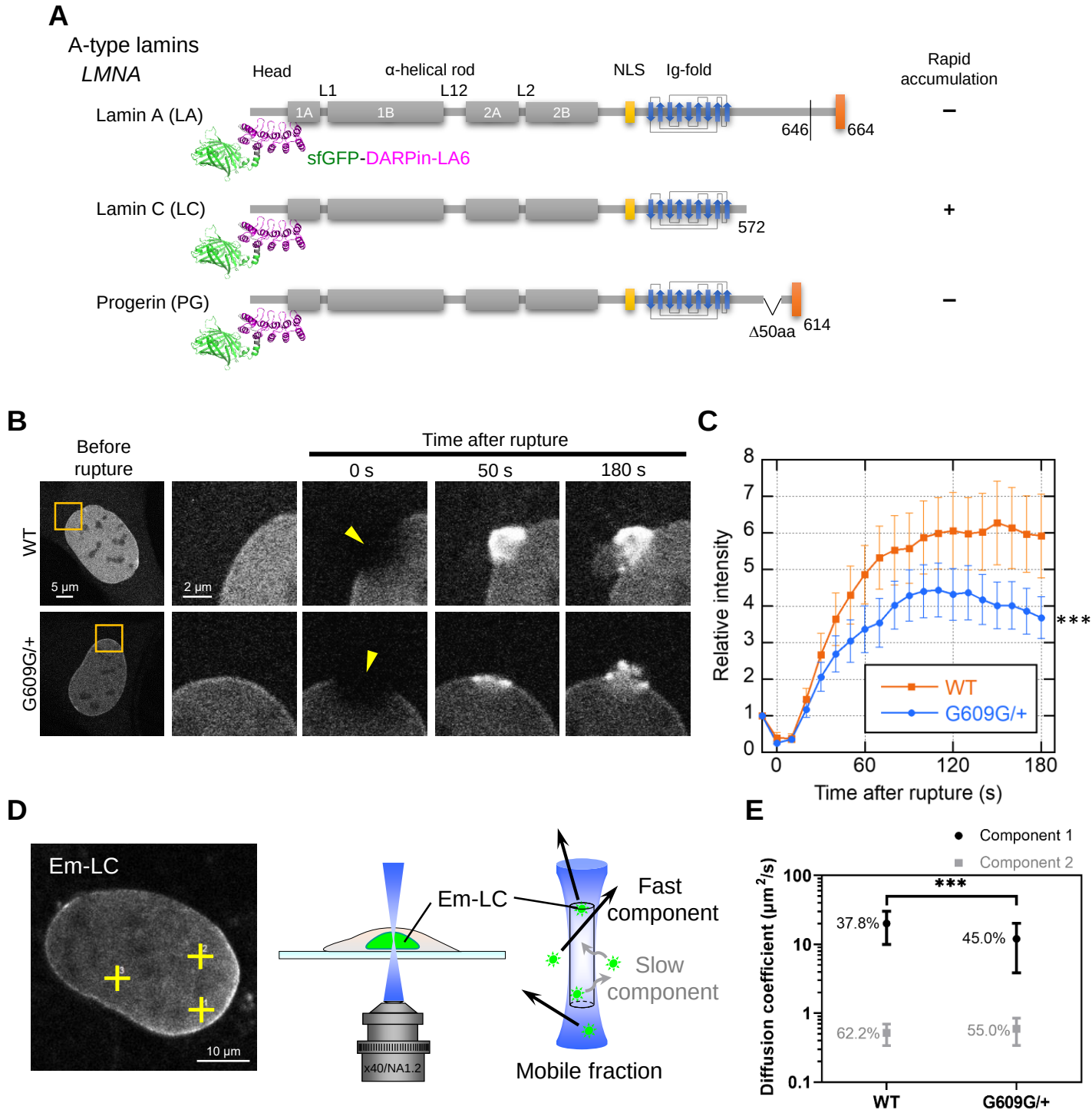
A
A-type lamins
LMNA
Head
α-helical rod
NLS
Ig-fold
Rapid accumulation
L1
L12
L2
1A
1B
2A
2B
Lamin A (LA)
646
664
–
sfGFP-DARPin-LA6
Lamin C (LC)
572
+
Progerin (PG)
Δ50aa
614
–
B
Before rupture
Time after rupture
0 s
50 s
180 s
WT
G609G/+
5 µm
2 µm
C
Relative intensity
Time after rupture (s)
WT
G609G/+
***
D
Em-LC
10 µm
Em-LC
Fast component
Slow component
Mobile fraction
x40/NA1.2
E
Component 1
Component 2
Diffusion coefficient (µm²/s)
***
37.8%
45.0%
62.2%
55.0%
WT
G609G/+

Fig. 3

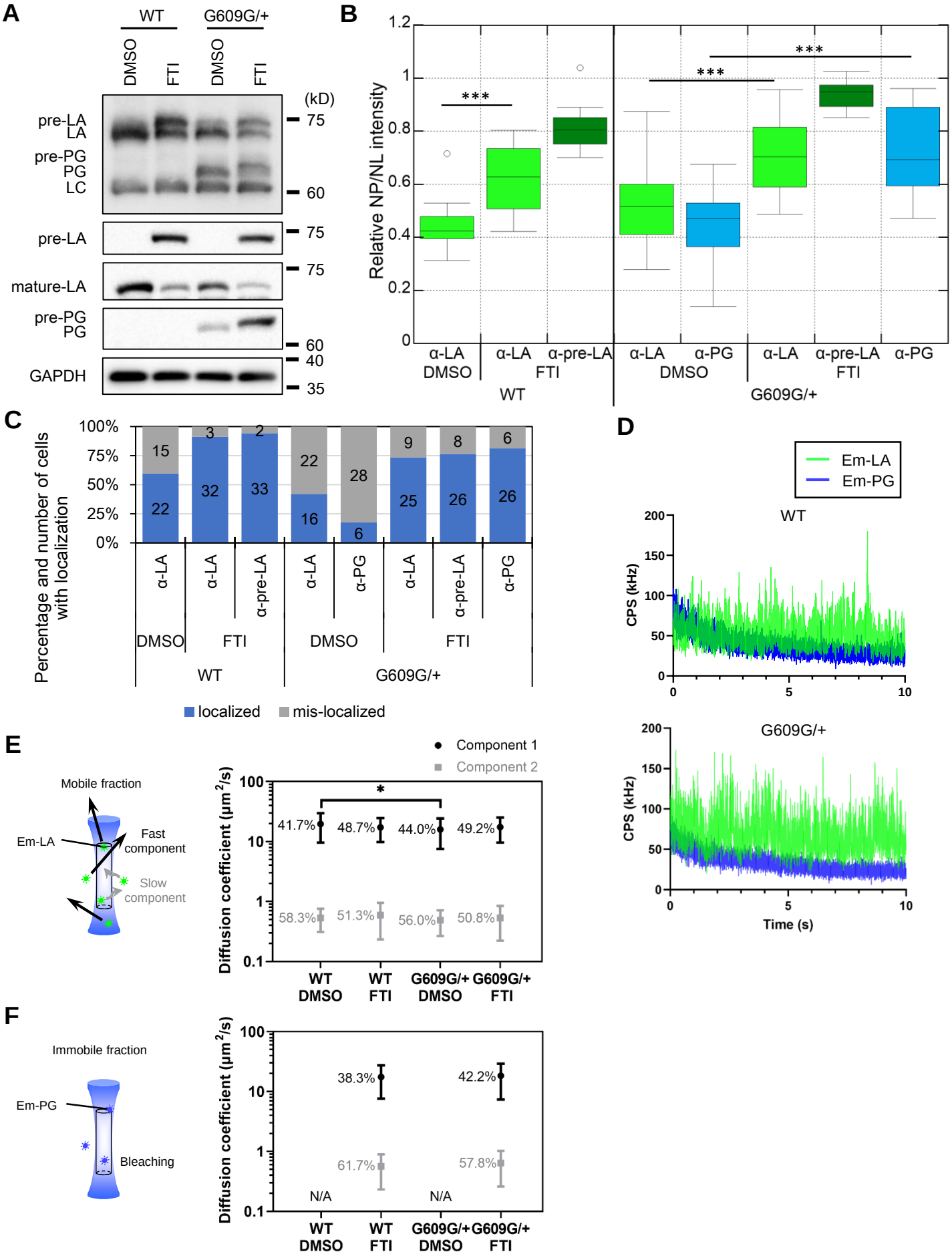
A
WT
G609G/+
DMSO
FTI
DMSO
FTI
(kD)
pre-LA
LA
pre-PG
PG
LC
75
60
pre-LA
75
mature-LA
75
pre-PG
PG
60
40
GAPDH
35
B
Relative NP/NL intensity
1.2
1
0.8
0.6
0.4
0.2
0
***
***
***
α-LA
α-LA
α-pre-LA
α-LA
α-PG
α-LA
α-pre-LA
α-PG
DMSO
FTI
DMSO
FTI
WT
G609G/+
C
Percentage and number of cells with localization
100%
75%
50%
25%
0%
15
22
3
32
2
33
22
16
28
6
9
25
8
26
6
26
α-LA
α-LA
α-pre-LA
α-LA
α-PG
α-LA
α-pre-LA
α-PG
DMSO
FTI
DMSO
FTI
WT
G609G/+
localized
mis-localized
D
Em-LA
Em-PG
WT
CPS (kHz)
200
150
100
50
0
0
5
10
G609G/+
CPS (kHz)
200
150
100
50
0
0
5
10
Time (s)
E
Mobile fraction
Em-LA
Fast component
Slow component
Component 1
Component 2
Diffusion coefficient (μm²/s)
100
10
1
0.1
*
41.7%
48.7%
44.0%
49.2%
58.3%
51.3%
56.0%
50.8%
WT DMSO
WT FTI
G609G/+ DMSO
G609G/+ FTI
F
Immobile fraction
Em-PG
Bleaching
Diffusion coefficient (μm²/s)
100
10
1
0.1
38.3%
42.2%
61.7%
57.8%
N/A
N/A
WT DMSO
WT FTI
G609G/+ DMSO
G609G/+ FTI

Fig. 4

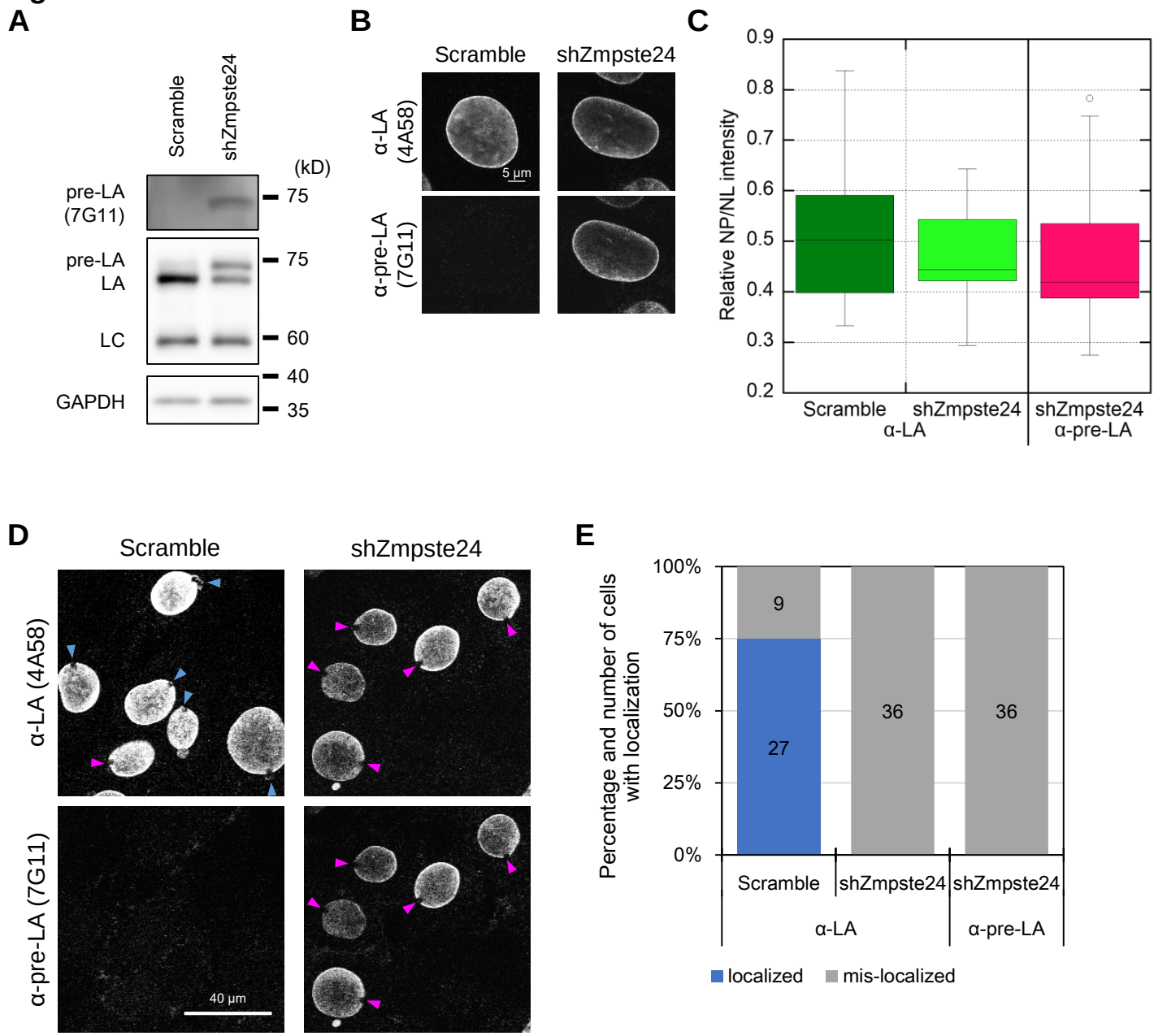
A
Scramble
shZmpste24
(kD)
pre-LA
(7G11)
75
pre-LA
LA
75
LC
60
40
GAPDH
35
B
Scramble
shZmpste24
α-LA
(4A58)
5 μm
α-pre-LA
(7G11)
C
Relative NP/NL intensity
0.9
0.8
0.7
0.6
0.5
0.4
0.3
0.2
Scramble
shZmpste24
α-LA
shZmpste24
α-pre-LA
D
Scramble
shZmpste24
α-LA (4A58)
α-pre-LA (7G11)
40 μm
E
Percentage and number of cells with localization
100%
75%
50%
25%
0%
9
27
36
36
Scramble
shZmpste24
shZmpste24
α-LA
α-pre-LA
localized
mis-localized

Fig. 5

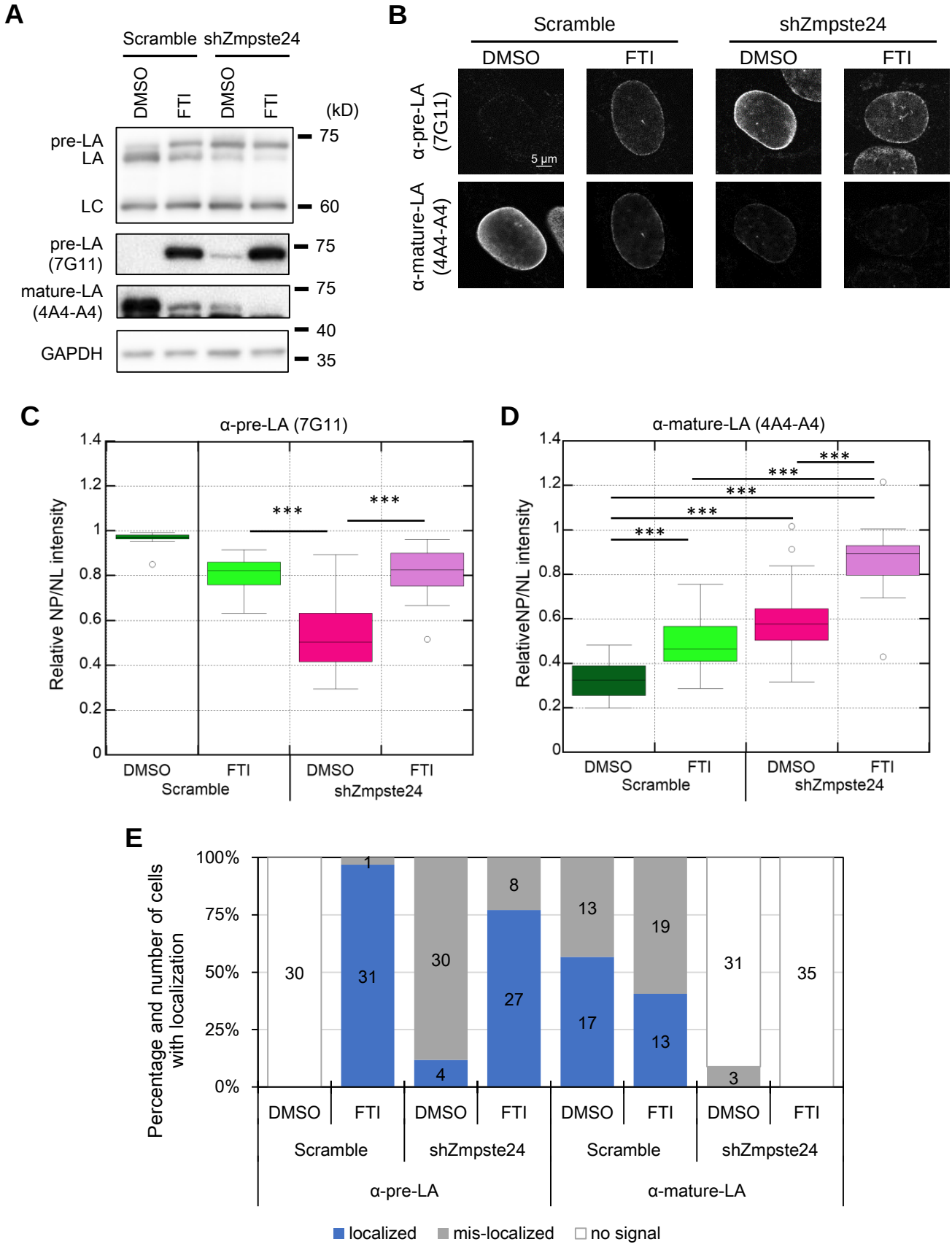
A
Scramble
shZmpste24
DMSO
FTI
DMSO
FTI
(kD)
pre-LA
LA
LC
pre-LA
(7G11)
mature-LA
(4A4-A4)
GAPDH
75
60
75
75
40
35
B
Scramble
shZmpste24
DMSO
FTI
DMSO
FTI
α-pre-LA
(7G11)
α-mature-LA
(4A4-A4)
5 μm
C
α-pre-LA (7G11)
Relative NP/NL intensity
1.4
1.2
1
0.8
0.6
0.4
0.2
0
***
***
DMSO
FTI
DMSO
FTI
Scramble
shZmpste24
D
α-mature-LA (4A4-A4)
RelativeNP/NL intensity
1.4
1.2
1
0.8
0.6
0.4
0.2
0
***
***
***
***
***
DMSO
FTI
DMSO
FTI
Scramble
shZmpste24
E
Percentage and number of cells
with localization
100%
75%
50%
25%
0%
30
1
31
30
4
8
27
13
17
19
13
31
3
35
DMSO
FTI
DMSO
FTI
DMSO
FTI
DMSO
FTI
Scramble
shZmpste24
Scramble
shZmpste24
α-pre-LA
α-mature-LA
localized
mis-localized
no signal

Fig. 6

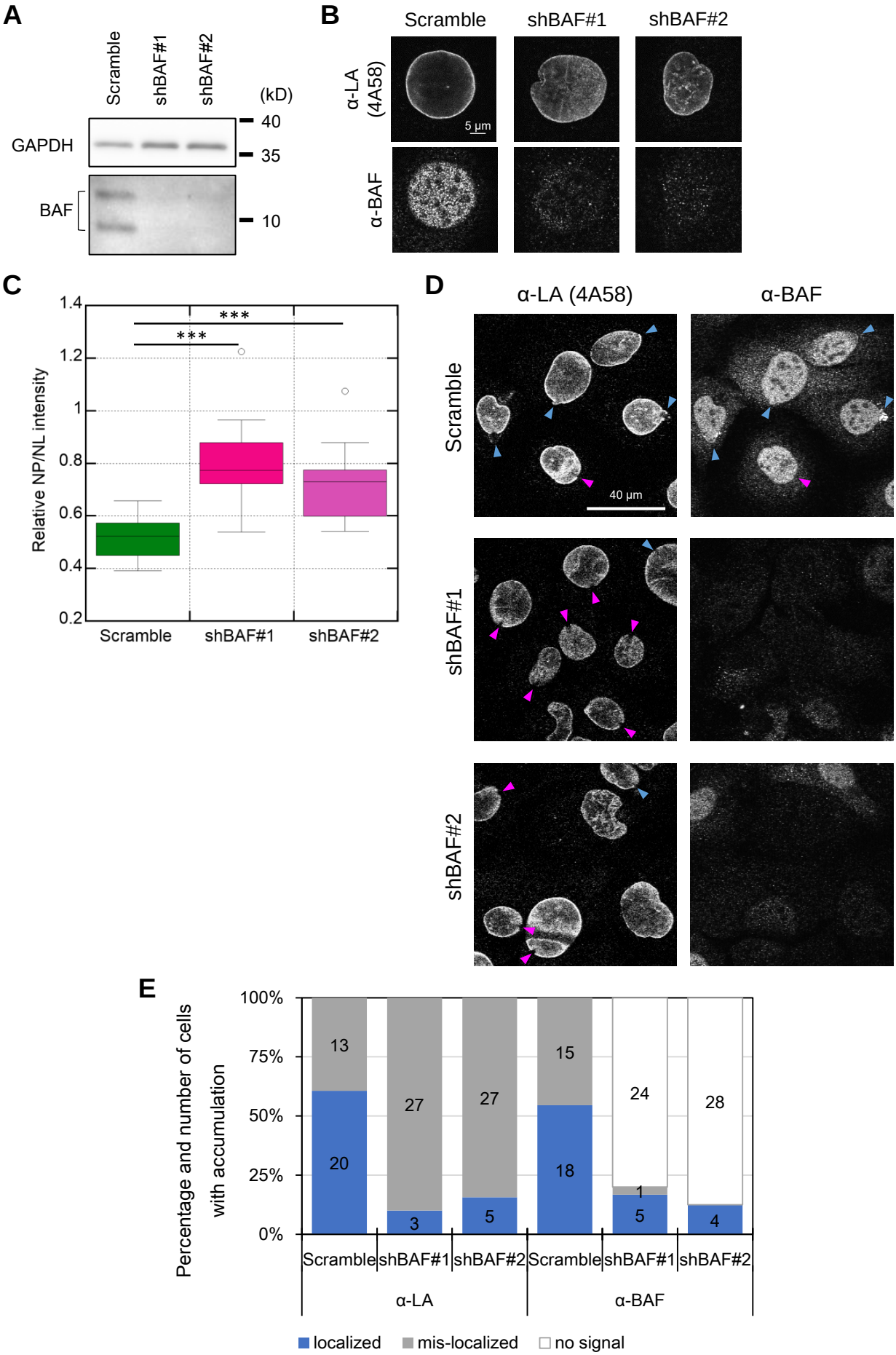
A
Scramble
shBAF#1
shBAF#2
(kD)
GAPDH
BAF
40
35
10
B
Scramble
shBAF#1
shBAF#2
α-LA (4A58)
α-BAF
5 μm
C
Relative NP/NL intensity
1.4
1.2
1
0.8
0.6
0.4
0.2
***
***
Scramble
shBAF#1
shBAF#2
D
α-LA (4A58)
α-BAF
Scramble
shBAF#1
shBAF#2
40 μm
E
Percentage and number of cells with accumulation
100%
75%
50%
25%
0%
13
20
27
3
27
5
15
18
24
1
5
28
4
Scramble
shBAF#1
shBAF#2
Scramble
shBAF#1
shBAF#2
α-LA
α-BAF
localized
mis-localized
no signal

Fig. 7

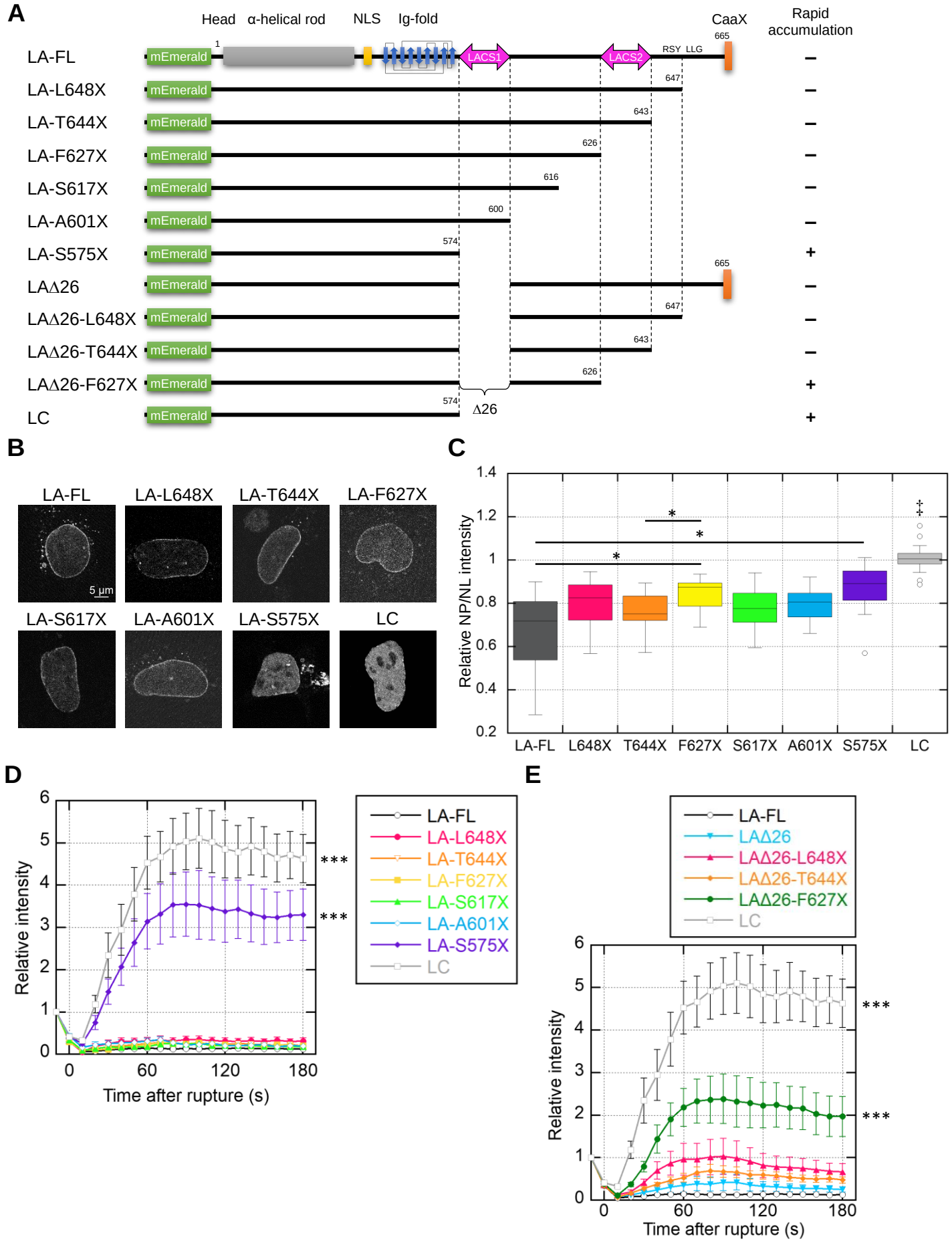
A
Head
α-helical rod
NLS
Ig-fold
CaaX
Rapid accumulation
LA-FL
LA-L648X
LA-T644X
LA-F627X
LA-S617X
LA-A601X
LA-S575X
LAΔ26
LAΔ26-L648X
LAΔ26-T644X
LAΔ26-F627X
LC
mEmerald
LACS1
LACS2
RSY LLG
Δ26
B
5 μm
C
Relative NP/NL intensity
D
Relative intensity
Time after rupture (s)
E
LAΔ26
LAΔ26-L648X
LAΔ26-T644X
LAΔ26-F627X

Fig. 8

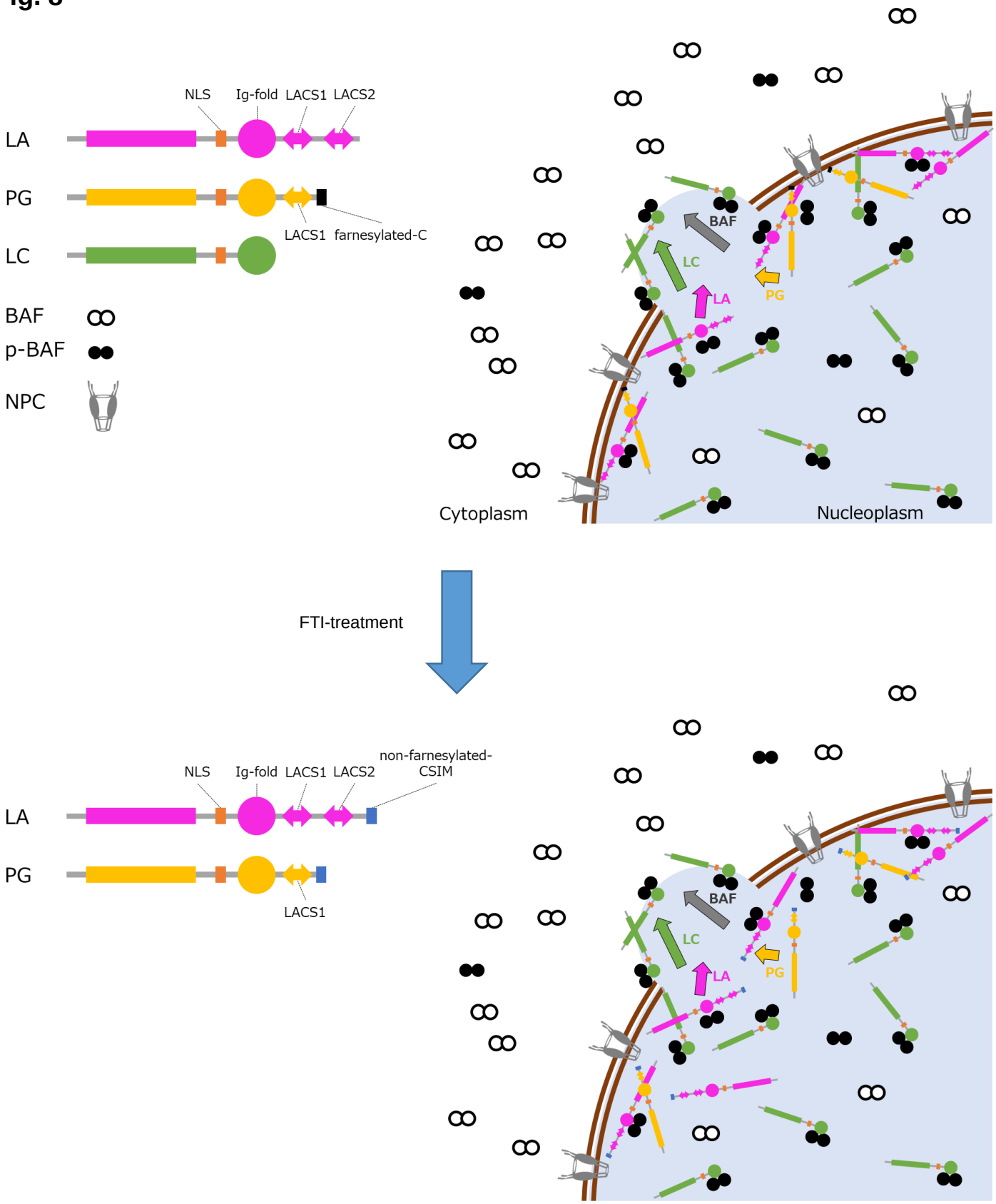
NLS
Ig-fold
LACS1
LACS2
LA
PG
LACS1
farnesylated-C
LC
BAF
p-BAF
NPC
BAF
LC
LA
PG
Cytoplasm
Nucleoplasm
FTI-treatment
non-farnesylated-CSIM
NLS
Ig-fold
LACS1
LACS2
LA
PG
LACS1
BAF
LC
LA
PG

Table S1. Phenotype characterization of WT and G609G/+ MEFs

	WT (n = 118 cells, 129 nuclei)	G609G/+ (n = 116 cells, 131 nuclei)	P value
DNA			0.465
normal	122 (94.6%)	120 (91.6%)	
mis-shapen	7 (5.4%)	11 (8.4%)	
NLS-sfCherry			0.102
nuclear-localized	110 (93.2%)	114 (98.3%)	
ruptured	8 (6.8%)	2 (1.7%)	
α-LB1			0.212
normal distributed	125 (96.9%)	130 (99.2%)	
mis-localized	4 (3.1%)	1 (0.8%)	
α-cGAS			1
not accumulated	129 (100%)	131 (100%)	
accumulated	0 (0%)	0 (0%)	

Table S2. Oligonucleotides used in this study

No.	Name	Sequence (5' to 3')
1	shSte24#1-TRCN0000366641_S	CCGGCTGGATGCTCTTCCGGTTATTCTCGAGAATAACCGGAAGAGCATCCAGTTTTTG
2	shSte24#1-TRCN0000366641_AS	AATTCAAAAACTGGATGCTCTTCCGGTTATTCTCGAGAATAACCGGAAGAGCATCCAG
3	shBanf1#1-TRCN0000124958_Fw	CCGGTGGCCAGTTTCTGGTGCTAAACTCGAGTTTAGCACCAGAAACTGGCCATTTTTG
4	shBanf1#1-TRCN0000124958_Rv	AATTCAAAAATGGCCAGTTTCTGGTGCTAAACTCGAGTTTAGCACCAGAAACTGGCCA
5	shBanf1#2-TRCN0000124955_Fw	CCGGGACAAGGCTTATGTGGTCCTTCTCGAGAAGGACCACATAAGCCTTGTCTTTTTG
6	shBanf1#2-TRCN0000124955_Rv	AATTCAAAAAGACAAGGCTTATGTGGTCCTTCTCGAGAAGGACCACATAAGCCTTGTC
7	pX459V2-Fw	GAATTCTAACTAGAGCTCGCTGATCAGCCTCG
8	pX459V2-Rv	TGGGCCAGGATTCTCCTCGACGTCAC
9	if_mCherry_Fw	GAGAATCCTGGCCCAATGGTGAGCAAGGGCGAGGAGG
10	if_mCherry_Rv	CTCTAGTTAGAATTCTCACTTGTACAGCTCGTCCATGCCGCCGG
11	sgRosa26-1_s	CACCGACTCCAGTCTTTCTAGAAGA
12	sgRosa26-1_as	AAACTCTTCTAGAAAGACTGGAGTC
13	if_LA promoter_Fw	ATGCATTAGTTATTAATTGCCTCGAAAAACCAAAAAAAG
14	if_LA promoter_Rv	GACCGGTAGCGCTAGCCCGCTGTGACGGGGTCTCCATG
15	if_mLA_Fw	ATGGAGACCCCGTCACAGCGG
16	if_mLA_Rv	AACCGGTAGCGCTAGCCATGATGCTGCAGTTCTGGG
17	mLA-to-PG_Fw	CAGAGCTCCCAGAACTGCAGC
18	mLA-to-PG_Rv	TCTGGGAGCTCTGGGCTCCCGCTCCACCG
19	mLA-L648X_Fw (mature)	CACCCGCTCCTACTAGCTGGGCAACTCC
20	mLA-L648X_Rv (mature)	GGAGTTGCCCAGCTAGTAGGAGCGGGTG
21	mLA-T644X_Fw	GACAACCTAGTCTAACGCTCCTACCTC
22	mLA-T644X_Rv	GAGGTAGGAGCGTTAGACTAGGTTGTC
23	mLA-F627X_Fw	GTCACTCGAAGCTGACGCAGTGTGGGG
24	mLA-F627X_Rv	CCCCACACTGCGTCAGCTTCGAGTGAC
25	mLA-S617X_Fw	CCTCTGGCTCTTGAGCCTCCAGTGTC
26	mLA-S617X_Rv	GACACTGGAGGCTCAAGAGCCAGAGG
27	mLA-A601X_Fw	GCTGACAAGGCTTGAGGTGGAGCGGGAG
28	mLA-A601X_R2	CTCCCGCTCCACCTCAAGCCTTGTCAGCAG
29	mLA-S575X_Fw	CACTGCAGCGGCTAGGGGGACCCCGC
30	mLA-S575X_Rv	GCGGGGTCCCCCTAGCCGCTGCAGTG
31	if_mLA-del575-600_Fw	CAGCGGCGCCGGTGGAGCGGGAGCCC
32	if_mLA-del575-600_Rv	CCACCGGCGCCGCTGCAGTGGGAACCAC
33	if_Rosa26L-mLA_Fw	GTCTTTCTAGCCTTAATTAATGCCTCGAAAAACCAAAA
34	if_mLA-bGHpA-Rv	GAGGTCGACCAATTGTTACATGATGCTGCAGTTCTG
35	if_bGHpA_Fw	CAATTGGTCGACCTCGACCTCGACTG
36	if_Rosa26R-bGHpA_Rv	GCGGCCGCCGCGCCCACGCGTTCCCCAGCATGCC
37	if_Nsi-BGHpA_Fw	GGCAGCCGCCGCTGAATGCATCAATTGGTCGACCTCGACCTCGACTGT
38	if_mLA-to-mLC_Rv	TCAGCGGCGGCTGCCACTCACACGGTGGTGATGGAGGAGCTCTTCT

See Materials and methods. Oligonucleotides were synthesized by Integrated DNA Technologies (IDT) or Sigma-Aldrich.

Fig. S1

A

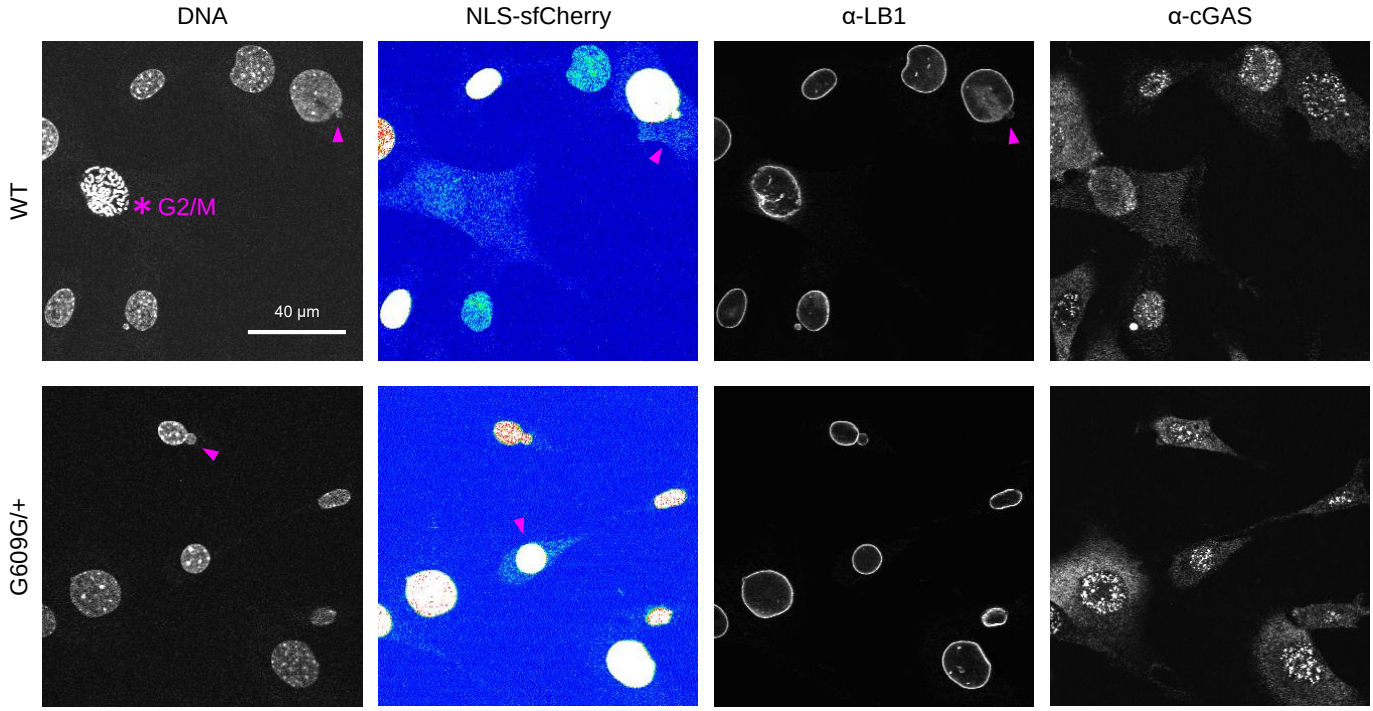
DNA
NLS-sfCherry
α-LB1
α-cGAS
WT
G609G/+
* G2/M
40 µm

B

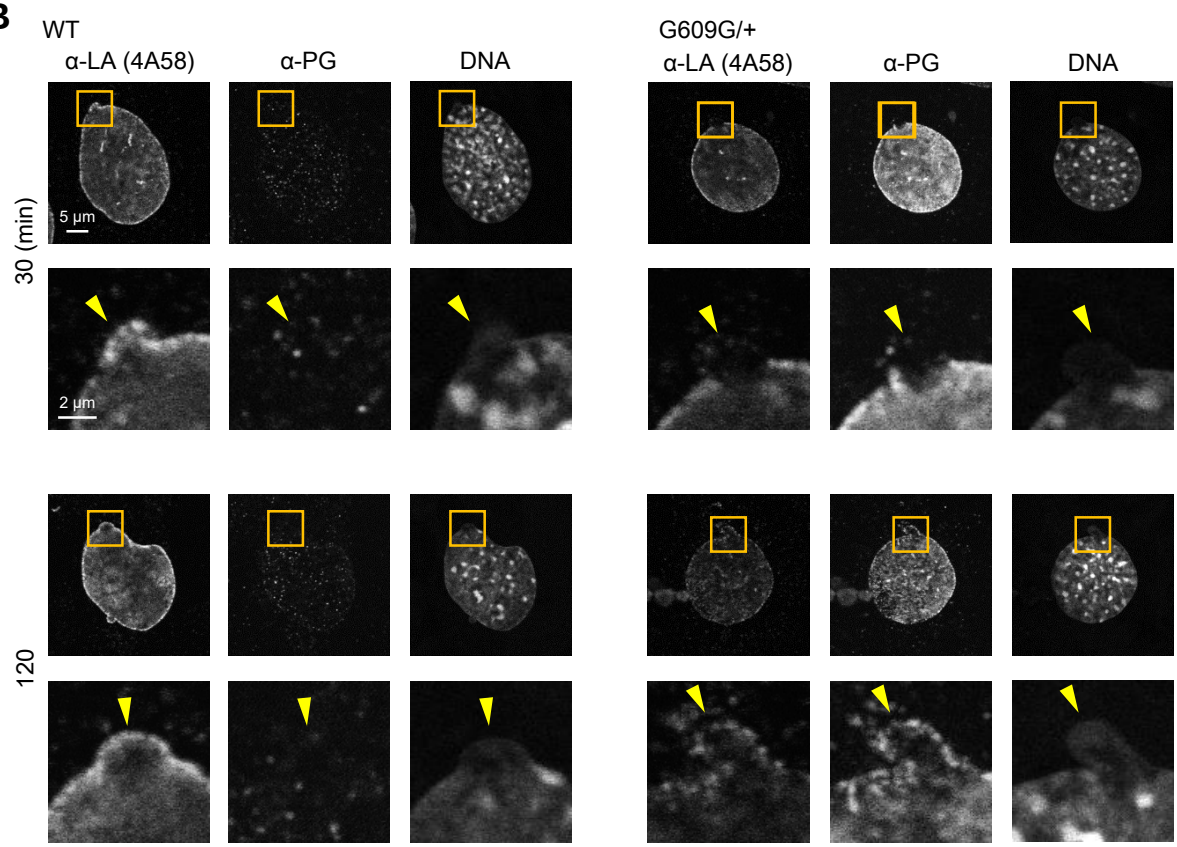
WT
G609G/+
α-LA (4A58)
α-PG
DNA
30 (min)
120
5 µm
2 µm

Fig. S2

A

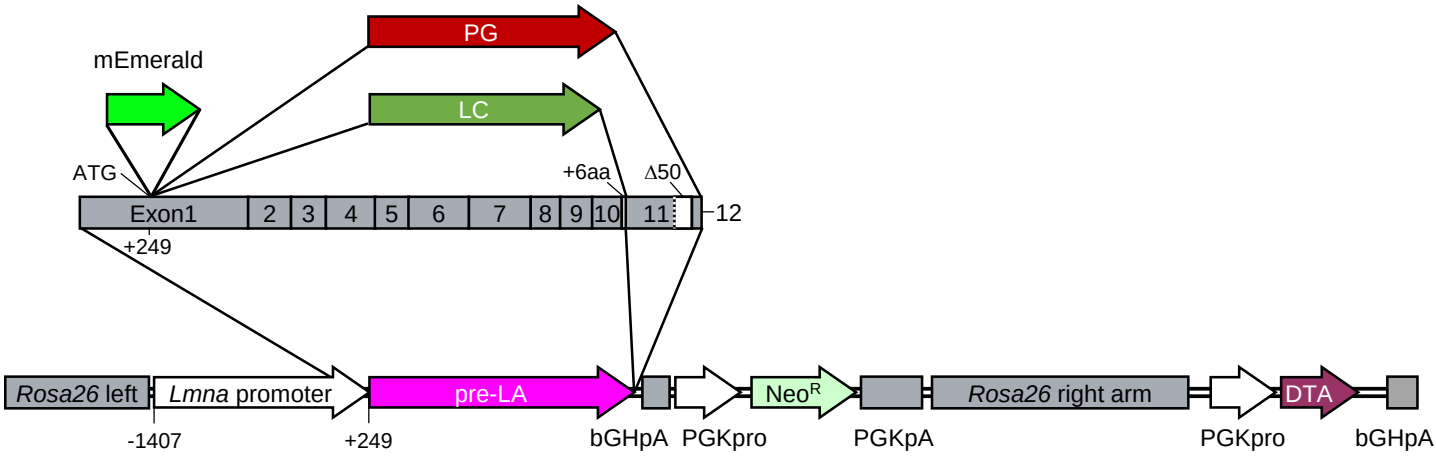
PG
mEmerald
LC
ATG
+6aa
Δ50
Exon1
2
3
4
5
6
7
8
9
10
11
12
+249
Rosa26 left
Lmna promoter
pre-LA
NeoR
Rosa26 right arm
DTA
-1407
+249
bGHpA
PGKpro
PGKpA
PGKpro
bGHpA

B

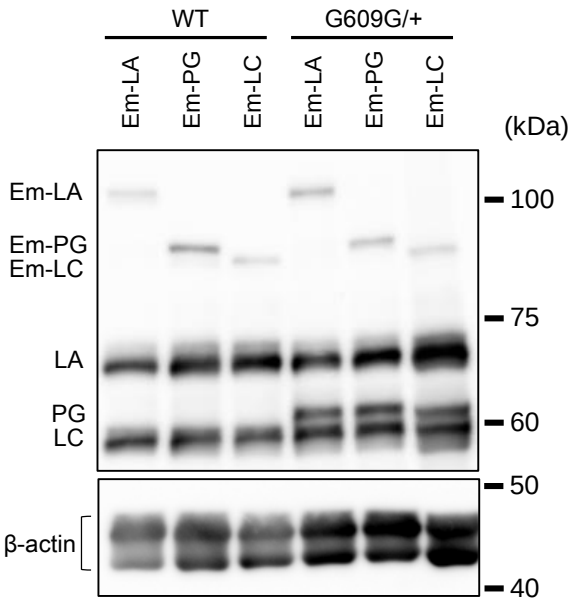
WT
G609G/+
Em-LA
Em-PG
Em-LC
Em-LA
Em-PG
Em-LC
(kDa)
Em-LA
Em-PG
Em-LC
LA
PG
LC
β-actin
100
75
60
50
40

Fig. S3

A

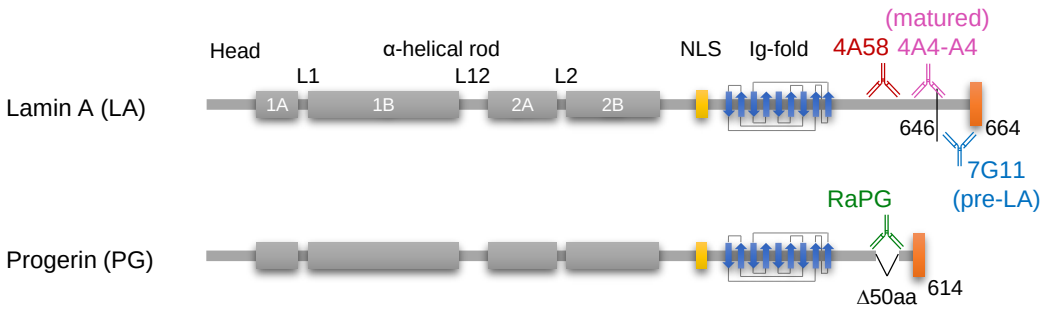
Head
α-helical rod
NLS
Ig-fold
(matured)
4A58
4A4-A4
L1
L12
L2
Lamin A (LA)
1A
1B
2A
2B
646
664
7G11
(pre-LA)
RaPG
Progerin (PG)
Δ50aa
614

B

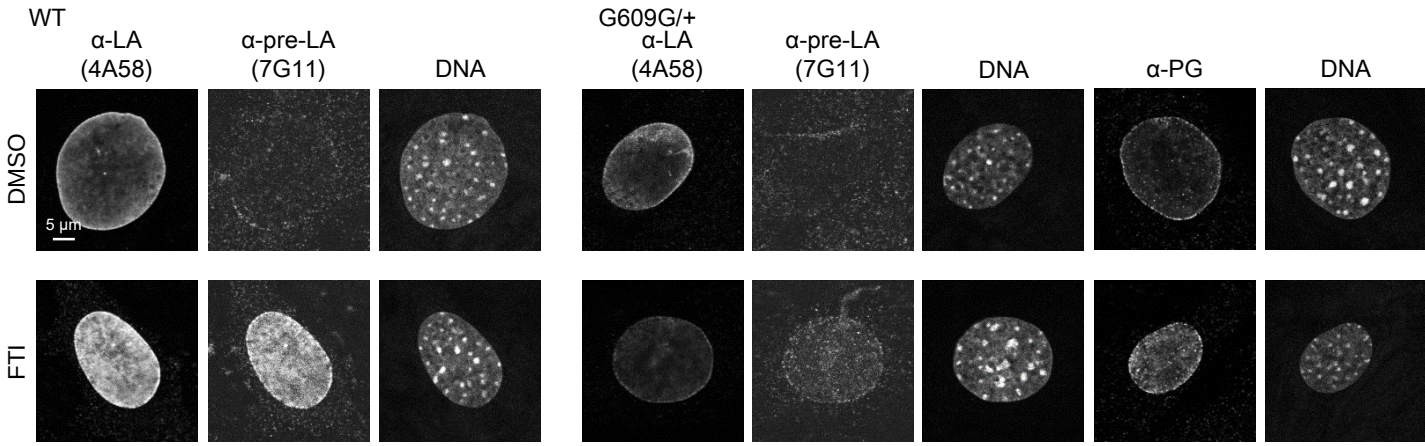
WT
α-LA
(4A58)
α-pre-LA
(7G11)
DNA
G609G/+
α-LA
(4A58)
α-pre-LA
(7G11)
DNA
α-PG
DNA
DMSO
FTI
5 μm

C

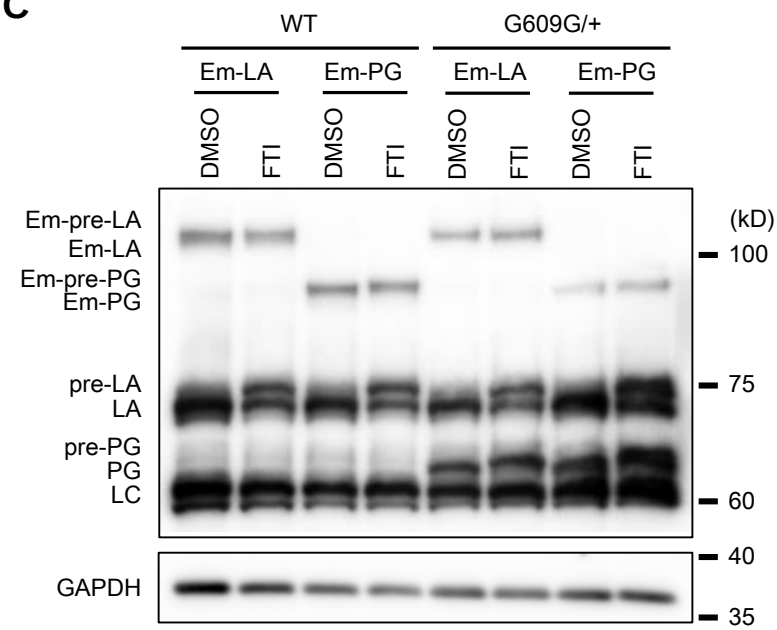
WT
G609G/+
Em-LA
Em-PG
Em-LA
Em-PG
DMSO
FTI
DMSO
FTI
DMSO
FTI
DMSO
FTI
Em-pre-LA
Em-LA
Em-pre-PG
Em-PG
pre-LA
LA
pre-PG
PG
LC
GAPDH
(kD)
100
75
60
40
35

Fig. S4

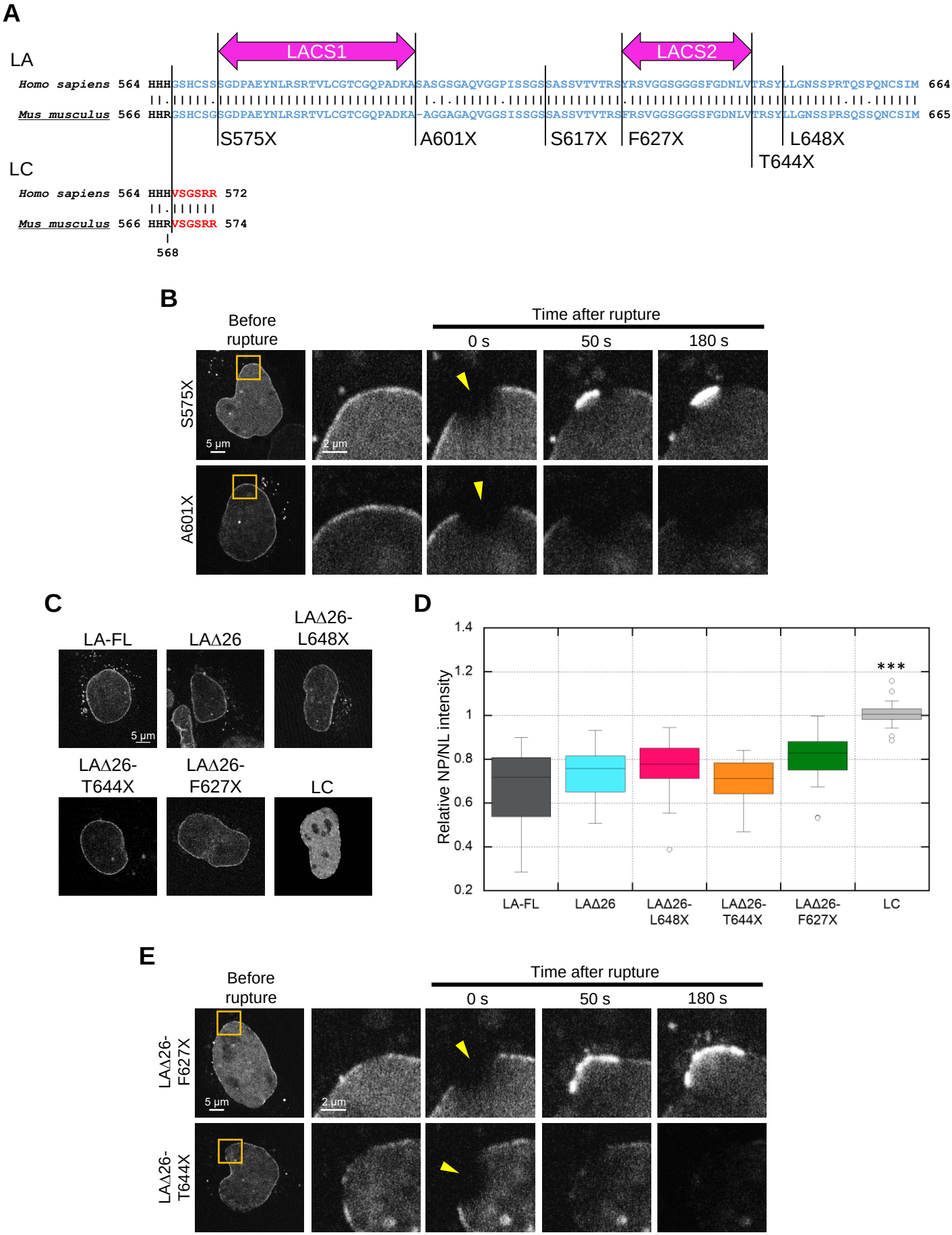
A
LA
LACS1
LACS2
Homo sapiens 564 HHHGSHCSSSGDPAEYNLRSRTVLCGTCGQPADKASASGSGAQVGGPISSGSSASSVTVTRSYRSVGGSGGGSFGDNLVTRSYLLGNSSPRTQSPQNCSIM 664
Mus musculus 566 HHRGSHCSGSGDPAEYNLRSRTVLCGTCGQPADKA-AGGAGAQVGGSISSGSSASSVTVTRSFRSVGGSGGGSFGDNLVTRSYLLGNSSPRSQSSQNCSIM 665
S575X
A601X
S617X
F627X
L648X
T644X
LC
Homo sapiens 564 HHHVSGSRR 572
Mus musculus 566 HHRVSGSRR 574
568
B
Before rupture
Time after rupture
0 s
50 s
180 s
S575X
A601X
5 µm
2 µm
C
LA-FL
LAΔ26
LAΔ26-L648X
LAΔ26-T644X
LAΔ26-F627X
LC
5 µm
D
Relative NP/NL intensity
1.4
1.2
1
0.8
0.6
0.4
0.2
***
LA-FL
LAΔ26
LAΔ26-L648X
LAΔ26-T644X
LAΔ26-F627X
LC
E
Before rupture
Time after rupture
0 s
50 s
180 s
LAΔ26-F627X
LAΔ26-T644X
5 µm
2 µm